Cell

Structure and Function of Stator Units of the Bacterial Flagellar Motor

Graphical Abstract

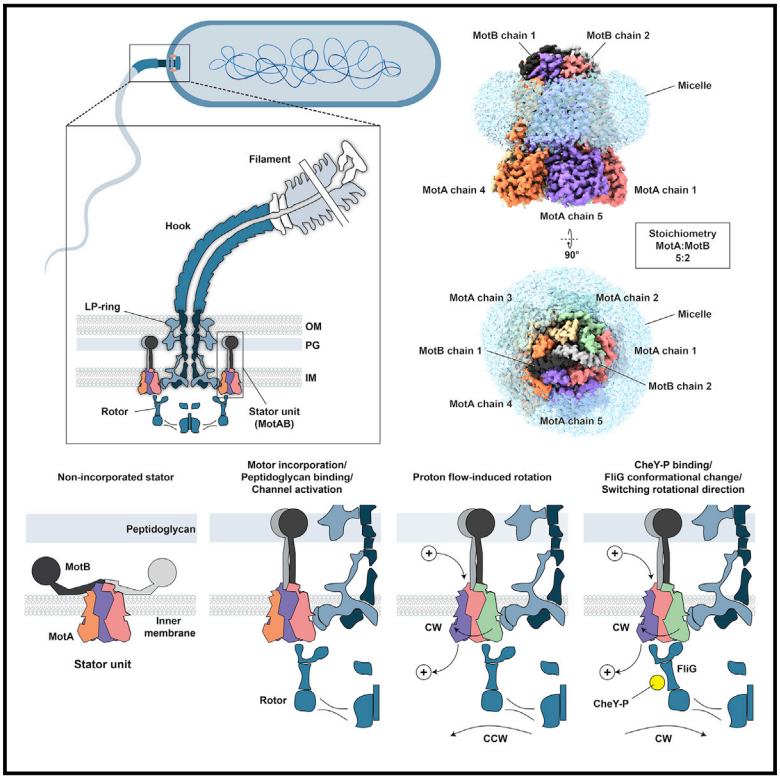

Highlights

- Structure of MotAB flagellar stator unit in different functional states by cryo-EM
- 5:2 stoichiometry is conserved across the MotAB/PomAB family
- Conformational changes upon protonation
- $MotB_2$ drives rotation of surrounding $MotA_5$, which engages the rotor to generate torque

Authors

Mònica Santiveri, Aritz Roa-Eguiara, Caroline Kühne, ..., Howard C. Berg, Marc Erhardt, Nicholas M.I. Taylor

Correspondence

nicholas.taylor@cpr.ku.dk

In Brief

Structures of the MotAB stator unit reveal how its conformational changes, coupled to ion transport, provide torque to power the rotation of the bacterial flagellum.

Santiveri et al., 2020, Cell *183*, 244–257
October 1, 2020
https://doi.org/10.1016/j.cell.2020.08.016

CellPress

CellPress

Cell

Article

Structure and Function of Stator Units of the Bacterial Flagellar Motor

Mònica Santiveri,[1] Aritz Roa-Eguiara,[1] Caroline Kühne,[2] Navish Wadhwa,[3,4] Haidai Hu,[1] Howard C. Berg,[3,4] Marc Erhardt,[2] and Nicholas M.I. Taylor[1,5,*]

[1]Structural Biology of Molecular Machines Group, Protein Structure & Function Program, Novo Nordisk Foundation Center for Protein Research, Faculty of Health and Medical Sciences, University of Copenhagen, Blegdamsvej 3B, 2200 Copenhagen, Denmark
[2]Institut für Biologie/Bakterienphysiologie, Humboldt-Universität zu Berlin, Philippstrasse 13, 10115 Berlin, Germany
[3]Department of Molecular and Cellular Biology, Harvard University, 16 Divinity Avenue, Cambridge, MA 02138, USA
[4]Rowland Institute at Harvard, Harvard University, 100 Edwin H. Land Boulevard, Cambridge, MA 02142, USA
[5]Lead Contact
*Correspondence: nicholas.taylor@cpr.ku.dk
https://doi.org/10.1016/j.cell.2020.08.016

SUMMARY

Many bacteria use the flagellum for locomotion and chemotaxis. Its bidirectional rotation is driven by a membrane-embedded motor, which uses energy from the transmembrane ion gradient to generate torque at the interface between stator units and rotor. The structural organization of the stator unit (MotAB), its conformational changes upon ion transport, and how these changes power rotation of the flagellum remain unknown. Here, we present ~3 Å-resolution cryoelectron microscopy reconstructions of the stator unit in different functional states. We show that the stator unit consists of a dimer of MotB surrounded by a pentamer of MotA. Combining structural data with mutagenesis and functional studies, we identify key residues involved in torque generation and present a detailed mechanistic model for motor function and switching of rotational direction.

INTRODUCTION

Numerous bacteria use rotating flagella to propel themselves (Berg and Anderson, 1973; Silverman and Simon, 1974). The ability to move is crucial for bacterial survival and pathogenicity (Duan et al., 2013; Haiko and Westerlund-Wikström, 2013). The flagellum is made of a long external filament functioning as a propeller; a flexible linking structure, the hook; and a motor embedded in the cell envelope (Berg, 2003; DeRosier, 1998; Morimoto and Minamino, 2014; Nakamura and Minamino, 2019) (Figure 1A). The ion-powered rotary motor consists of a rotor surrounded by a ring of stator protein complexes (MotAB) that power its rotation (Coulton and Murray, 1978; Khan et al., 1988, 1991, 1992). The motor is bidirectional: chemotactic signaling can cause a conformational change in the rotor, known as "switching" (Minamino et al., 2019), which results in a change of the rotational direction of the motor.

Of note, the prokaryotic rotary motor stator unit family (Lai et al., 2020) of which MotAB is the best-studied example is apart from the rotary ATPase family the only known motor that uses energy from the transmembrane (TM) ion gradient instead of ATP to generate mechanical work (Mandadapu et al., 2015). Unlike the rotary ATPases, for which great structural insight has been obtained in recent years (Kühlbrandt and Davies, 2016), the mechanism of action of MotAB and stator units of other prokaryotic rotary motors remains poorly understood.

The stator units of the bacterial flagellar motor are embedded in the inner membrane, allowing interaction with the motor and the formation of an ion channel (Coulton and Murray, 1978; Khan et al., 1988, 1991; 1992; Stader et al., 1986; Wilson and Macnab, 1988). They are in a plugged, inactive state and get activated upon motor incorporation and peptidoglycan binding (Hosking et al., 2006). Rotation of the rotor is powered by dispersion of an ion (generally H^+ or Na^+) motive force through the stator units (Hirota and Imae, 1983; Larsen et al., 1974). It has been proposed that ion binding by the stator unit induces a conformational change in the stator unit itself (Kojima and Blair, 2001). The stator unit protein MotA is thought to contact the FliG protein (through the torque helix ($Helix_{Torque}$) of the C-terminal domain $FliG_{CC}$), which forms part of the cytoplasmic C-ring of the rotor. In this way, the proposed conformational changes in the stator unit are driving rotation of the rotor (Kojima and Blair, 2001; Lee et al., 2010; Minamino et al., 2019; Zhou et al., 1998a). A large body of genetic data is available on mutations in the motor that affect movement and are characterized as Mot^- (non-motile, i.e., deficient in motor rotation) or Che^- (no chemotaxis, which can be caused by a deficiency in switching rotational direction) (Yamaguchi et al., 1986). All previously described mutations in the stator unit proteins are Mot^- and not Che^-. This indicates that switching of the rotational direction is caused solely by structural changes in the rotor. The same conformational changes in the stator unit that power rotation of the rotor in the counterclockwise (CCW) direction, must therefore

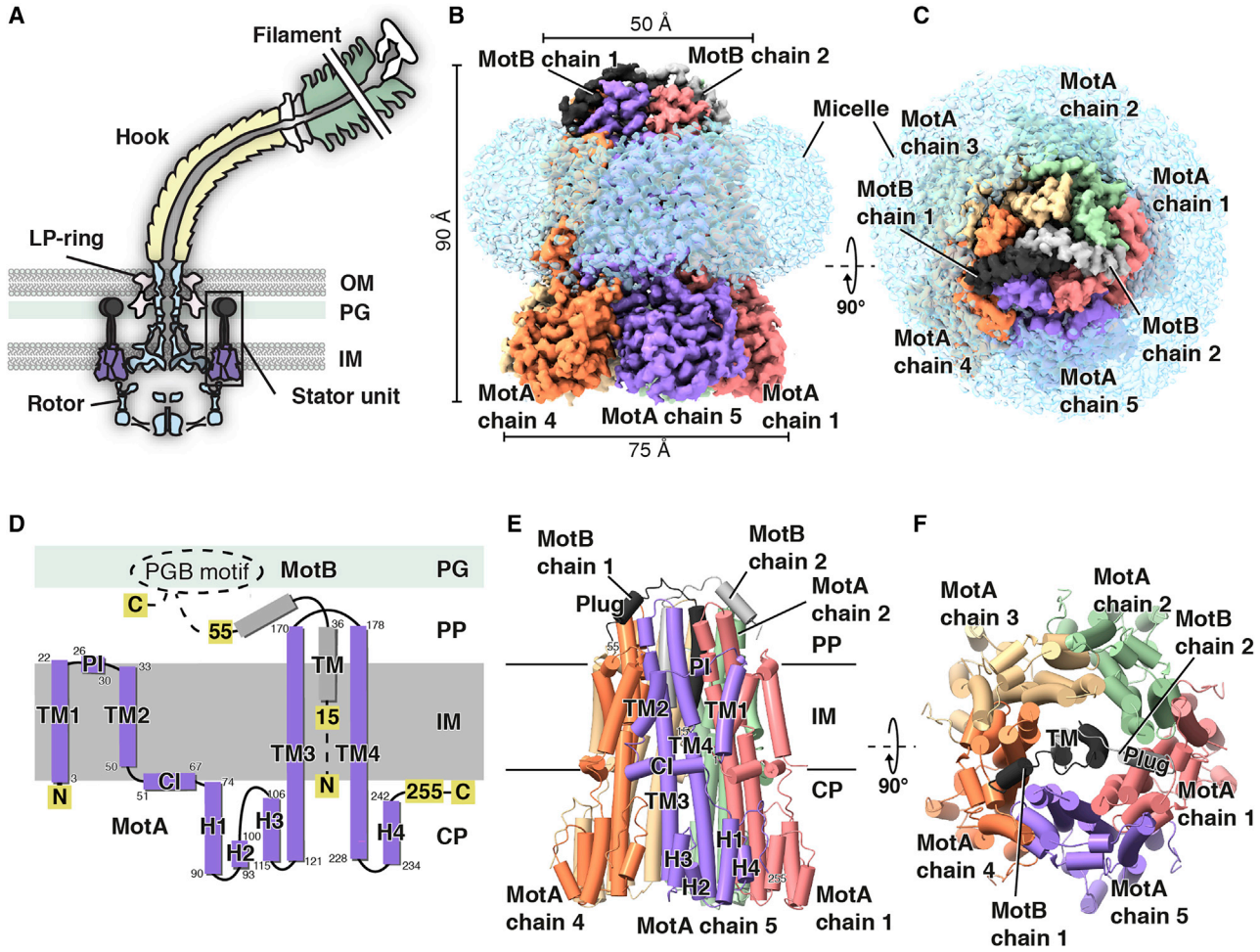

Figure 1. Architecture and Topology of the Flagellar Stator Unit $MotA_5$-$MotB_2$

(A) Organization of the bacterial flagellar motor (in gram-negative bacteria). MotA: purple, MotB: dark gray, rotor with export apparatus: light blue, LP-ring: pink, hook: pale yellow, filament: green. Adapted from reference (Evans et al., 2014). OM, outer membrane; PG, peptidoglycan; IM, inner membrane.

(B and C) Side (B) and top (C, periplasmic side) views of the cryo-EM map of the *Cj*MotAB stator unit in a detergent micelle.

(D) Topology organization of MotA (purple) and MotB (gray) subunit. Dashed lines indicate regions not resolved in this study. The OmpA-like domain containing the PGB motif is indicated as an ellipse. TM helices are numbered from TM1 to TM4. Interface helices are PI for the Periplasmic Interface helix and CI for the Cytosolic Interface helix. Cytosolic helices are numbered from H1 to H5. PG, peptidoglycan; IM, inner membrane; PP, periplasm; CP, cytoplasm; PGB motif, peptidoglycan-binding motif.

(E and F) Side (E) and top (F) views of the atomic model representation. Subunit color code is the same as in (B) and (C). Secondary structure elements are labeled for MotA chain 5 and MotB chain 1 in (E) and for MotB chain 2 in (F).

See also Figures S2, S5, S6, and S7 and Video S1.

also power rotation in the clockwise (CW) direction. Upon switching, it is thought that $FliG_{CC}$ makes a 180° turn relative to the stator unit, which allows the rotor to turn in the other direction (Lee et al., 2010).

The stator unit is a complex of two membrane proteins, MotA and MotB (for the H^+-driven motor) (Tang et al., 1996). MotA contains four TM helices and a large cytoplasmic domain that is proposed to interact with the rotor (Blair and Berg, 1991; Dean et al., 1984; Zhou et al., 1995). MotB contains a single TM helix followed by a large periplasmic domain, which can bind peptidoglycan (Kojima et al., 2018; Roujeinikova, 2008). The MotB TM domain contains a universally conserved aspartate residue (D22 in *Campylobacter jejuni*, D33 in *Salmonella enterica*), which is thought to be directly involved in proton transport (Zhou et al., 1998b). Directly following the MotB TM domain is a region known as the plug (Hosking et al., 2006). Incorporation of the stator unit in the motor is coupled to the unplugging of the stator unit and peptidoglycan domain dimerization, allowing it to bind peptidoglycan. Crosslinking, biochemical, and genetic data for both MotAB and PomAB (a Na^+-dependent stator unit) have allowed the identification of residues involved in complex formation and function (Braun and Blair, 2001; Sato and Homma, 2000; Sharp et al., 1995a, 1995b; Tang et al., 1996). Based on these experiments, the stoichiometry of the MotAB stator unit has been suggested to be 4:2. However, this is based on the facts that MotB must at least be a dimer and that the MotA:MotB ratio is at least

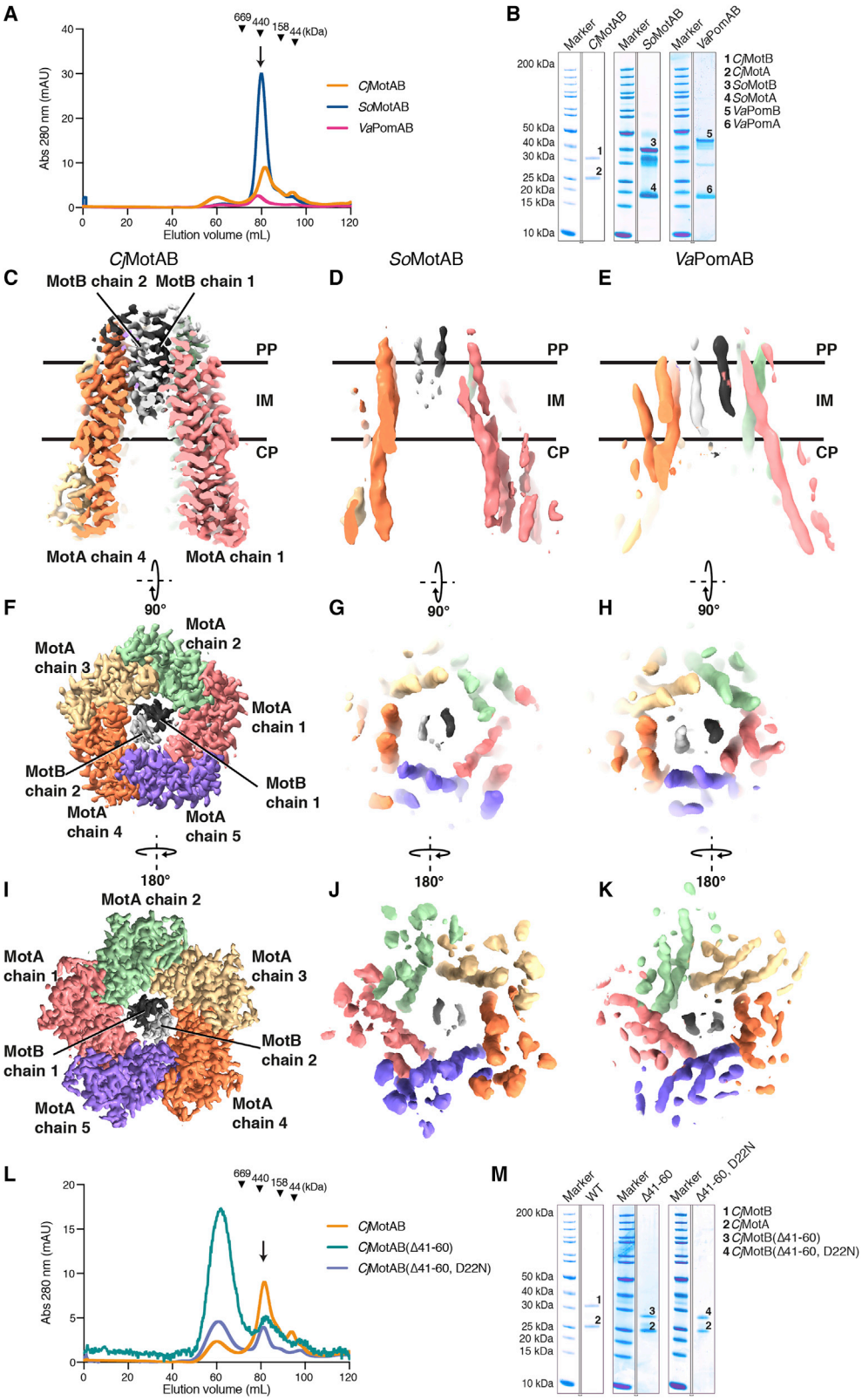

(legend on next page)

2:1 (Kojima and Blair, 2004). Negative stain electron microscopy structures of *Vibrio alginolyticus* PomAB (Yonekura et al., 2011) and *Aquifex aeolicus* MotA (Takekawa et al., 2016) have been reported, but due to the limited resolution these do not provide information on stator unit stoichiometry or mechanism.

MotAB shows some sequence homology to energizing proteins of other systems, which have been proposed to be stator units of prokaryotic rotary motors (Lai et al., 2020) such as ExbBD (Kojima and Blair, 2001), TolQR (Cascales et al., 2001), and AglRQS (Sun et al., 2011). The stoichiometry of ExbBD was uncertain and different experiments reported 4:1, 4:2, 5:2, and 6:3 stoichiometries (Celia et al., 2016; Maki-Yonekura et al., 2018; Sverzhinsky et al., 2015). However, a recent high-resolution structure of ExbBD shows a clear 5:2 stoichiometry (Celia et al., 2019), which is consistent with the existence of ExbB pentamers in the native *Escherichia coli* membrane (Chorev et al., 2018).

Despite great advances in the last decades concerning flagellar motor function, we still do not understand the structural and mechanistic basis of ion transport, channel (un)plugging, and torque generation. To help answer these questions, we determined ~3 Å cryoelectron microscopy (cryo-EM) structures of MotAB in different states, as well as lower-resolution structures of several other stator units. Our structures demonstrate a 5:2 stoichiometry for the stator unit complex MotAB, which we show is conserved across the MotAB/PomAB family, and reveal the structural basis of the autoinhibitory plugging of non-incorporated stator units. Furthermore, we infer the structural changes upon proton transport that are driving rotor rotation from the structures of different functional states and validate our structural results using extensive mutagenic analysis of the flagellar stator unit complex. Finally, based on our structural and functional results, we provide a detailed model for motor powering and rotational direction switching.

RESULTS

The Flagellar Stator Unit Is a 5:2 Complex

To obtain detailed insight into the mechanism of flagellar stator unit function, we tested the expression and purification of eight H^+- and Na^+-dependent stator units of seven different organisms (Figure S1). Of the eight protein complexes, six could be purified after detergent solubilization. For three of these (Figures 2A and 2B), we obtained cryo-EM reconstructions, with the best resolution (3.1 Å) for *C. jejuni* MotAB (*Cj*MotAB) (Figure S2; Table S1). The maps obtained for *Cj*MotAB allowed building of an atomic model for the nearly complete MotA protein and for the TM helix and plug of MotB (Figures 1B–1F, S2, S3, S4, and S5). Therefore, *Cj*MotAB was used as a model system to investigate the structural mechanism of the stator unit. We validated our structures using prior crosslinking, mutational, and tryptophan scanning data of the *E. coli* stator unit (Figures S6A–S6F). Structure determination of *Shewanella oneidensis* MotAB (*So*MotAB) and *V. alginolyticus* PomAB (*Va*PomAB) was complicated by preferential orientation of the protein in the ice but still allowed clear stoichiometry determination (Figures 2C–2K). We found that *Cj*MotAB forms a 5:2 complex, as do *So*MotAB and *Va*PomAB, suggesting that MotAB stoichiometry is conserved across all flagellar stator units. Furthermore, given the fact that the stoichiometry of ExbBD is identical (Celia et al., 2019), it is likely to be a property of the whole family of stator units of prokaryotic rotary motors.

Stator Unit Architecture

The flagellar stator unit has a truncated cone shape (widest at its cytoplasmic region) (Figure 1B; Video S1). Five copies of MotA cradle the single TM helices of the two copies of MotB. MotA TM helices 3 and 4 make direct interactions with MotB, and both these helices, which span the complete height of MotA, extend to the cytoplasmic domain.

The N-terminal part of MotA forms a parallelogram-like structure in the membrane. It consists of TM helix 1 (crossing from cytoplasm to periplasm), a linker including a 3_{10} helix lying horizontally at the periplasmic side of the membrane (periplasmic interface helix), TM helix 2, crossing from periplasm to cytoplasm, and finally the cytoplasmic interface helix, which then connects to the large cytoplasmic domain. Both horizontal helices are very polar on their external sides, and the cytoplasmic interface helix is very basic at its cytoplasmic side (Figures S7A–S7D).

The cytoplasmic domain of MotA is made up of two stretches of amino acid chains (residues 69–142 and 211–258) (Figure 1D). The surface conservation is generally low with two clear exceptions: the MotB interface and a highly conserved region at the

Figure 2. Purification and 5:2 Stoichiometry of MotAB Homologs and *Cj*MotAB Mutants

(A) Size-exclusion chromatography (SEC) profile of detergent-purified *C. jejuni* MotAB (*Cj*MotAB), *S. oneidensis* MotAB (*So*MotAB), and *V. alginolyticus* PomAB (*Va*PomAB) complexes. The fraction used for cryo-EM grid preparation is indicated with an arrow. Elution volumes of molecular weight standards are indicated with inverted triangles.

(B) The corresponding SDS-PAGE gels for (A) are shown. The images of the gels (one for each SEC run) have been aligned and rescaled according to their respective marker lanes. They have also been cropped and spliced together to show only the peak fraction indicated with an arrow in (A) and the corresponding marker. Expected molecular weights based on amino acids sequence are as follows: *Cj*MotA 28 kDa, *Cj*MotB-StrepII 32 kDa, *So*MotA 26.5 kDa, *So*MotB-StrepII 35 kDa, *Va*PomA 27.5 kDa, and *Va*PomB-StrepII 38 kDa.

(C, F, and I) (C) Side view of *Cj*MotAB. The same color code as in Figure 1 is used. (F) Same as (C) but top view. (I) Same as (C) but bottom view.

(D, G, and J) (D) Side view of *So*MotAB. The same color code as for *Cj*MotAB is used. (G) Same as (D) but top view. (J) Same as (D) but bottom view.

(E, H, and K) (E) Side view of *Va*PomAB. The same color code as for *Cj*MotAB is used. (H) Same as (E) but top view. (K) Same as (E) but bottom view.

(L) SEC profile of detergent-purified *Cj*MotAB, *Cj*MotAB(Δ41-60), and *Cj*MotAB(Δ41-60, D22N) complexes. The fraction used for cryo-EM grid preparation is indicated with an arrow. Elution volumes of molecular weight standards are indicated with inverted triangles. The *Cj*MotAB SEC run is the same as in (A).

(M) The corresponding SDS-PAGE gels for (L) are shown. The images of the gels have been rescaled, cropped, and spliced together as in (B); *Cj*MotAB (WT) marker and peak fraction lanes are the same as in (B). Expected molecular weight for both *Cj*MotB-StrepII mutants is 30 kDa.

See also Figures S1 and S7.

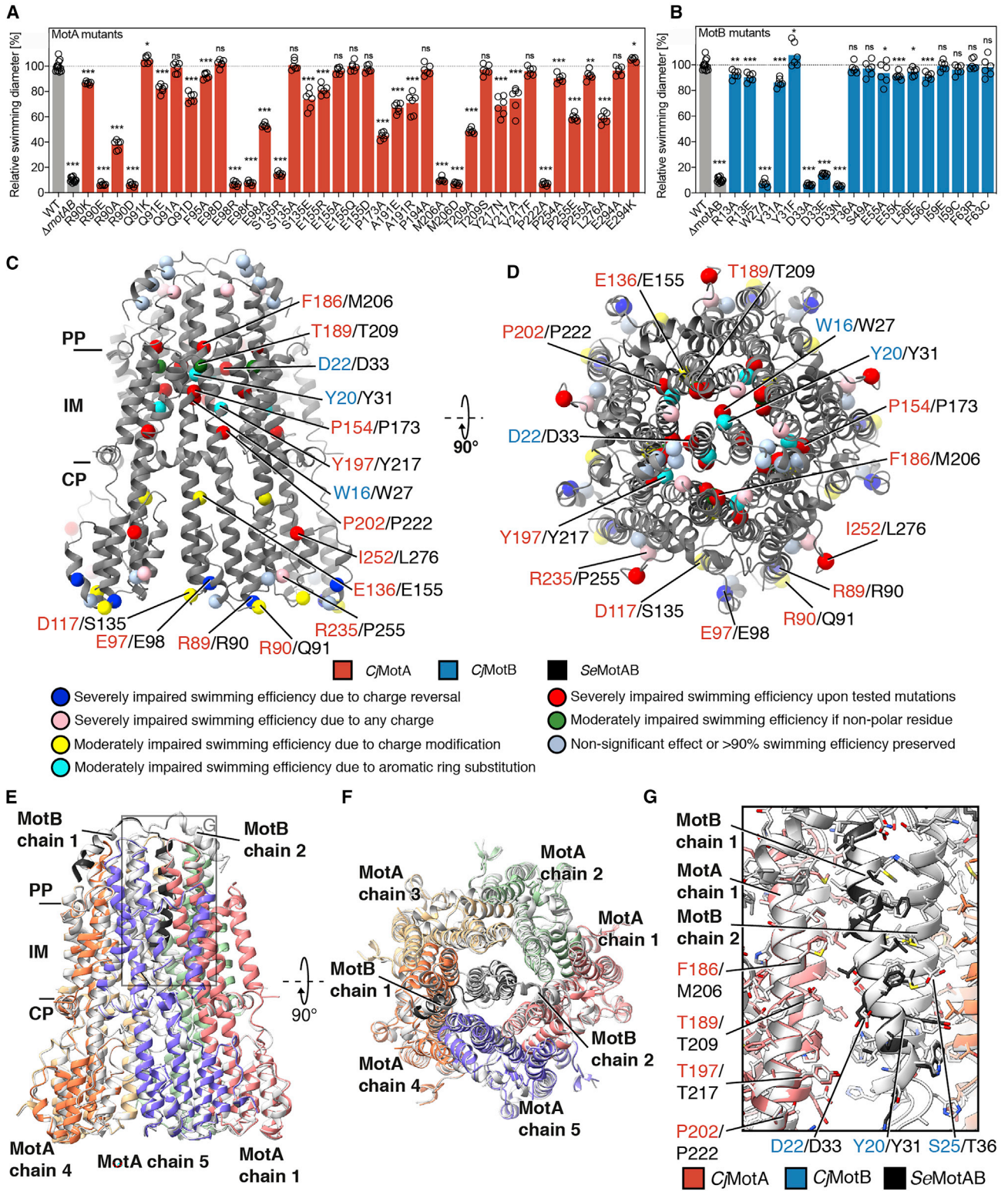

Figure 3. Swimming Motility Phenotype of *Se*MotAB Point Mutants

(A and B) The motility phenotypes of *S. enterica* MotA (A) and MotB (B) point mutants were analyzed using soft-agar motility plates containing 0.3% agar and quantified after a 3–4 h incubation at 37°C. The diameters of the motility swarm of each sample were measured using ImageJ and normalized to the wild type. The

(legend continued on next page)

base (most distal from the membrane) of the cytoplasmic domain of MotA, which extends slightly to the exterior of that protein (Figures 1D–1F and S7E–S7I). The latter region contains residues that have previously been shown to be important for torque generation (*Cj*MotB R89 and E97, corresponding to R90 and E98 in *E. coli*/*S. enterica*) (Zhou and Blair, 1997). Chromosomal point mutants of *S. enterica* MotA (*Se*MotA) R90 and E98 displayed a pronounced defect in motility when the charge of these residues was inverted (R90E, R90D and E98R, E98K) or the R90 arginine residue was mutated to the smaller amino acid alanine (Figure 3). The chromosomal point mutations of MotAB did not affect bacterial growth, suggesting that the observed motility defect was due to impaired motor function and not due to a general deficiency in cellular physiology, e.g., increased proton leakage. In support, charge reversal substitutions in these residues complement charge reversal mutants of oppositely charged residues in the FliG $Helix_{Torque}$ in *E. coli* (Zhou et al., 1998a). Therefore, we propose that this part of the structure contacts the rotor, and most likely FliG and its $Helix_{Torque}$, during torque generation (Figures S6G and S6H).

The inside of the MotA cytoplasmic region is extremely acidic (Figures S7A–S7D). Possibly, this region might act as a reservoir for taking up charges that have passed through the stator unit and/or might interact with the N-terminal tail of MotB, which is visible in our maps but is less ordered than the MotB TM helix (Figures S7J–S7L), and which contains various basic residues (Figure S1).

Stator Unit Channel Unplugging Activates the Ion Channel

To reveal the active state of the stator unit and the structural basis of unplugging, we determined the 3.0 Å structure of unplugged stator unit *Cj*MotAB(Δ41-60) (which has a deletion of the 20 equivalent MotB residues shown to be important for plugging in *E. coli* [Hosking et al., 2006]) (Figures 2L, 2M, and S3) and compared it to the full-length *Cj*MotAB structure (Figures 4A–4C; Video S2).

In the full-length structure, MotA interacts with extensions (or plugs, one per MotB chain) immediately C-terminal of the MotB TM helix. Seen from the periplasmic side of the channel, the plugs have pseudo-mirror symmetry, resulting in extensive interaction between both plugs at the crossover point (Figure 4A). After a short coil structure (residues 40–44), both plugs form a helix, which lies in between MotA subunits, with three MotA subunits on one side and two on the other. Deletion of the plug region in *E. coli* and *S. enterica* MotB results in a massive influx of protons into the cytoplasm and inhibition of cell growth (Hosking et al., 2006; Morimoto et al., 2010); therefore, the plug region is important to prevent proton leakage.

Comparing the structures of plugged and unplugged stator units, few conformational changes can be observed based on the lowest C_α root-mean-square deviation (rmsd) superposition (0.714 Å) (Figure 4A). For the larger residues of *Cj*MotB, changes are limited to different conformations of Y20, D22, and F23 in chain 1. Looking at the universally conserved *Cj*MotB D22 residue, we note that one (*Cj*MotB chain 1 D22) is mostly accessible (but pointing away) from the cytoplasmic interface (where we can observe solvent molecules), whereas the other (*Cj*MotB chain 2 D22) is interacting with MotA and not accessible to solvent, both in the plugged and unplugged structures (Figure 4B). This suggests that *Cj*MotB chain 1 D22, but not *Cj*MotB chain 2 D22, would be protonatable and/or able to interact with hydronium.

The MotB TM helix and the internal MotB-interacting surface of MotA are highly conserved (Figures S7E–S7I). Their interaction surfaces are almost purely hydrophobic, the only polar or charged residues are *Cj*MotA T155 and T189 and *Cj*MotB Y20, D22, and S25. With the exception of the first of these, the corresponding *Se*MotAB residues (*Se*MotA A174 and T210 and *Se*MotB Y31, D33, and T36) are also polar or charged (Figures 3E–3G). Of these, *Cj*MotA T189 and *Cj*MotB D22 are universally conserved and the polarity of *Cj*MotB S25 (which can be threonine in some stator units) is conserved as well (Figure S1). Interestingly, all these residues lie at the height of the cytoplasm-proximal base of the MotB TM helix, or put differently, at or below the height of the inner membrane-periplasm interface. Using swimming motility assays, we show that in *S. enterica*, only *Se*MotB D33 (*Cj*MotB D22) is absolutely required for motor function, but *Se*MotA T209A (*Cj*MotA T189) also displays severely decreased motility (while not affecting growth) (Figures 3A–3D; Table S2).

These observations suggest that an access pathway must exist for protons and/or hydronium ions to MotB chain 1 D22 from the periplasm in the unplugged structure, but not in the plugged structure. Such a pathway appears to exist from the side of MotA between chains 1 and 2, just above the TM region. In the unplugged structure, but not in the plugged structure, MotA chain 1 F186 appears to adopt two alternate positions (positions 1 and 2), as can be clearly seen in the map (Figures 4H–4J). Position 1 is the same as in the plugged structure. Position 2, which appears to be the most occupied, overlaps with the location that in the plugged structure is taken up by a solvent

bar graphs represent the mean of at least five biologically independent samples. Replicates are shown as individual data points, and statistical significances were determined by a two-tailed Student's t test (*p < 0.05, **p < 0.01, *p < 0.001, ns non-significant). WT, wild type.

(C and D) Swimming efficiency of the *S. enterica* point mutants, plotting the mutated residues as spheres on the *Cj*MotAB structure (gray) on the position of the C_α atoms of homologous residues in *C. jejuni* as side (C) and top (D) view. The corresponding *C. jejuni* residue is listed first and colored red (*Cj*MotA) or blue (*Cj*MotB), and the residue number of *Se*MotA or *Se*MotB that was mutated is shown in black. Mutants with non-significant effect or that preserve >90% swimming efficiency are not labeled for simplification.

(E) Structure of *Se*MotAB, modeled using Modeler based on the *Cj*MotAB cryo-EM structure, colored in the same color code as Figure 1. The *Cj*MotAB structure is colored in white. Residues *Se*MotA 107–123 and 279–295, corresponding to sequences linking H2 and H3 and a C-terminal extension, respectively, are not shown as they are not present in *Cj*MotA. The calculated C_α root-mean-square deviation (rmsd) between both structures is 0.760 Å.

(F) Same as (E) but top view (periplasmic side).

(G) Closeup of the squared region in (E) of the MotA-MotB interface of both stator units displaying the high conservation of the structure.

See also Figures S1 and S7and Table S2.

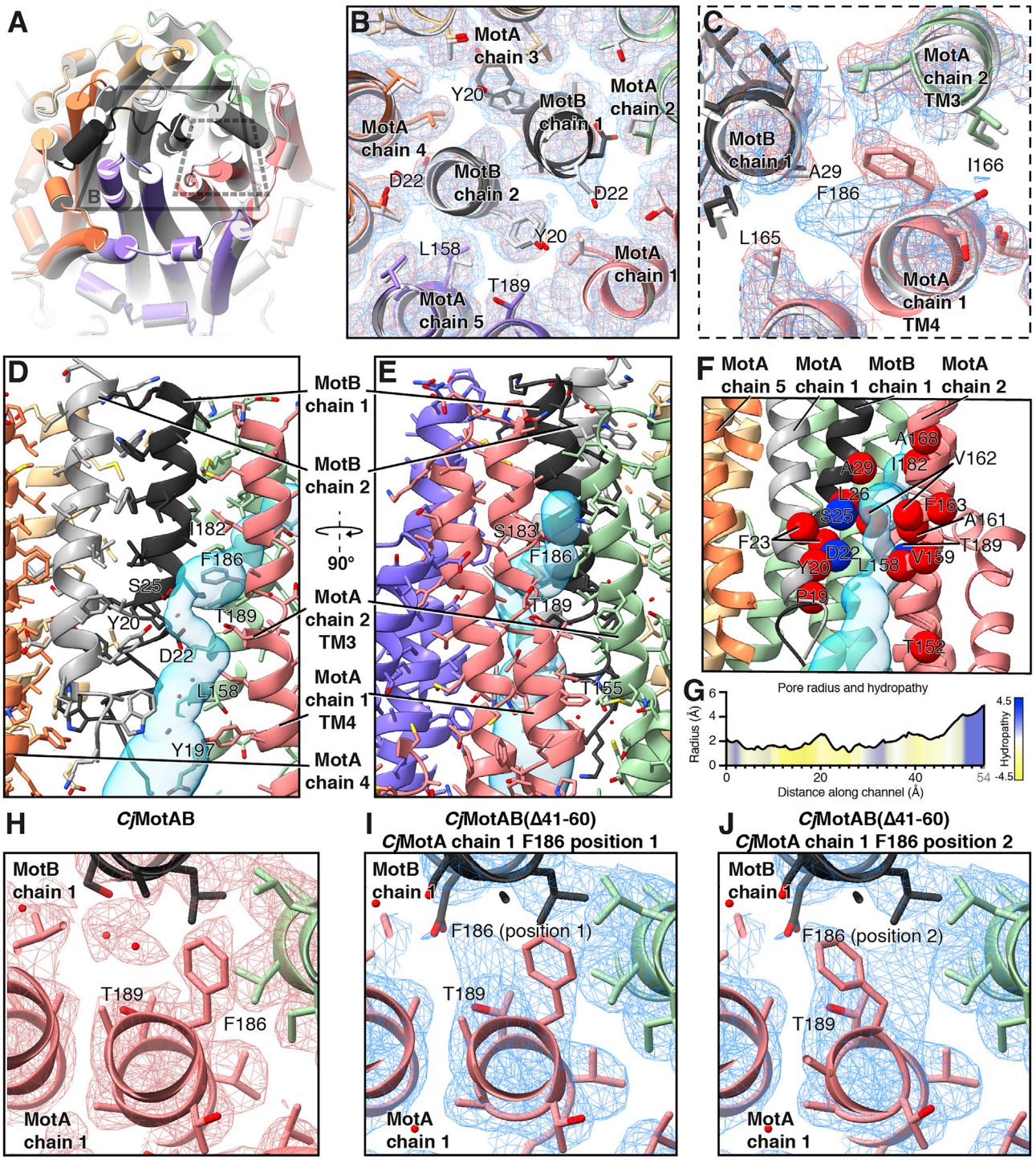

Figure 4. Conformational Changes of the Stator Unit upon Unplugging Open the Ion Channel, Access to Which Is Regulated by MotA Chain 1 F186 Flexibility

(A) Superposition of the plugged (colored, same color code as Figure 1) and unplugged (light gray) models on the periplasmic and TM region of the *Cj*MotAB complex.

(B and C) Closeup view from the periplasmic side of the unplugging effect on the TM plane at the D22 residue level of *Cj*MotB dimer (B) and at the MotA F186 residue (C). The density of the plugged and unplugged stator unit is shown in red and blue, respectively.

(D and E) Side (D) and front (E) views from within the membrane of the predicted channel for the unplugged conformation. A predicted solvent channel accessible to protons and hydronium ions calculated with Mole 2.5 (Pravda et al., 2018) (see STAR Methods) is shown in cyan.

(legend continued on next page)

molecule. This position is also in close proximity to MotB chain 1 S25 (and a solvent molecule that can be found near this residue in both structures), D22 and Y20 and MotA chain 1 T189. The polar residues outlined before appear to form a solvent-accessible channel (Figures 4D and 4E). The channel is lined with residues that have previously been shown to be important for ion transport (Onoue et al., 2019; Sudo et al., 2009; Terauchi et al., 2011) and/or are differentially conserved between H^+- and Na^+-dependent stator units (Figures 4F, 4G, and S1). *Cj*MotA F186 (*Se*MotA M206) is universally conserved hydrophobic residue (Figure S1). We found that mutations of *Se*MotA M206 to a small amino acid (M206A) or negatively charged amino acid (M206D) completely abrogated motility while not affecting growth (Figures 3A–3D; Table S2). This supports previous findings that M206 is involved in torque generation and proton translocation as well as pH-dependent stator assembly (Suzuki et al., 2019). We conclude that *Cj*MotA F186 is a hydrophobic residue shielding the periplasm from the hydrophilic channel of MotAB. We propose that unplugging increases flexibility of *Cj*MotA F186, allowing the passage of protons or hydronium ions through the channel.

Conformational Changes upon Protonation

To gain insight into the conformational changes that *Cj*MotAB undergoes upon proton transport, we determined the 3.0 Å cryo-EM structure of stator units that combine the unplugging mutation *Cj*MotB(Δ41-60) with a *Cj*MotB(D22N) mutation, mimicking protonation or hydronium binding of D22 (Figures 2L, 2M, and S3). The structure of *Cj*MotAB(Δ41-60, D22N) is extremely similar to *Cj*MotAB(Δ41-60) when observing the lowest C_α rmsd (0.297 Å) superposition, with one exception in MotB chain 1 (nomenclature based on structure alignment with lowest C_α rmsd not taking into account large-scale rotational movement). N22 is clearly in a different position compared to D22, pointing down toward the cytoplasmic interface, where we can also distinguish several putative solvent molecules (Figures 5 and S7M–S7O; Video S3). We conclude that proton or hydronium binding or release by *Cj*MotB chain 1 D22 establishes a small conformational change in and around this residue, strongly suggesting that this residue is directly involved in the shuttling of protons or hydronium ions.

DISCUSSION

A Rotational Model for Torque Generation

Stator units power the rotation of the flagellar motor using energy derived from the ion motive force. As mentioned, the only motors harnessing ion motive force to generate work found in nature are the stator unit family of prokaryotic rotary motors (exemplified by MotAB) and rotary ATPases. Our analysis combined with a plethora of prior structural and functional data show that the stator units interact with the rotor through the cytoplasmic domains of MotA to provide torque.

Two mechanisms can be proposed for how torque is generated: a "rotational" model, where MotA rotates around MotB, and a "large conformational change" model, where MotAB changes between two conformations without rotation of MotA around MotB.

Our results are fully consistent with a rotational mechanism of the stator unit, rather than a large conformational change mechanism. The C_α rmsd between *Cj*MotAB(Δ41-60) and *Cj*MotAB(Δ41-60, D22N) is 0.297 Å. It has been estimated that on the order of 37 (Lo et al., 2013) or 70 (Blair, 2003) ions are turned over per stator unit, per revolution of the rotor. From the geometry of the motor we calculate that the rotor needs to traverse an arc length of ~20–38 Å per ion. Consequently, the observed conformational changes are approximately two orders of magnitude smaller than the estimated arc length traversed per ion passage. Rotations of 36° or 72° of MotA around MotB, however, would traverse arc lengths of 24 and 47 Å, respectively. Therefore, we propose that MotAB, and most likely all stator unit proteins of prokaryotic rotary motors, uses a rotational mechanism to perform work.

An Inchworm Model for Powering of Rotation of MotA around MotB

Given the structural similarity of both unplugged structures and the number of ions per stator and per rotor rotation, it follows that rotation of MotA around MotB will occur in steps of either 36° (so that after each rotary step, MotB chain 2 would be in a position equivalent, with respect to MotA, to where MotB chain 1 was before the rotation, and vice versa) or 72° (with MotB chain 1 and chain 2 in the same equivalent positions, with respect to MotA, which they had before the rotation). The first model (36° rotation) is more likely, as in this model the universally conserved aspartate residue of both chains would transport ions alternately, while this would not happen in the second model. Superposing the *Cj*MotAB(Δ41-60) and *Cj*MotAB(Δ41-60, D22N) structures in this way and making the natural assumption that the hydrophobic MotA interior can only rotate around charge-neutralized MotB D22 readily points to a model for how rotation occurs at the molecular level (Figure 6; Videos S4 and S5). Note that charge neutralization by proton binding of a carboxylate group is also used in the Fo/Vo/Ao component of rotary ATPases, where protonation of an aspartate or glutamate residue on the c protein allows that residue's entry into the

(F) *Cj*MotAB stator unit (same color code as Figure 1) with the solvent-accessible volume of the ion channel (cyan) calculated with Mole 2.5 (Pravda et al., 2018) (see STAR Methods). Red spheres represent residues that are divergent between H^+- and Na^+-dependent stator units but that are conserved inside each group, while blue spheres represent highly conserved residues across both H^+- and Na^+-dependent stator units.
(G) Profile of channel radius and hydropathy for the calculated ion channel. The channel length is 54 Å and the bottleneck radius is 1.1 Å.
(H) Closeup view of *Cj*MotA chain 1 F186 in the plugged *Cj*MotAB structure in its only position.
(I) Closeup view of *Cj*MotA chain 1 F186 in the (unplugged) *Cj*MotAB(Δ41-60) structure in position 1 (same position as in the plugged structure).
(J) Closeup view of *Cj*MotA chain 1 F186 in the (unplugged) *Cj*MotAB(Δ41-60) structure in position 2. Note that there are also some conformational differences in the main chain around *Cj*MotA chain 1 F186.
See also Figures S3, S5, and S7 and Video S2.

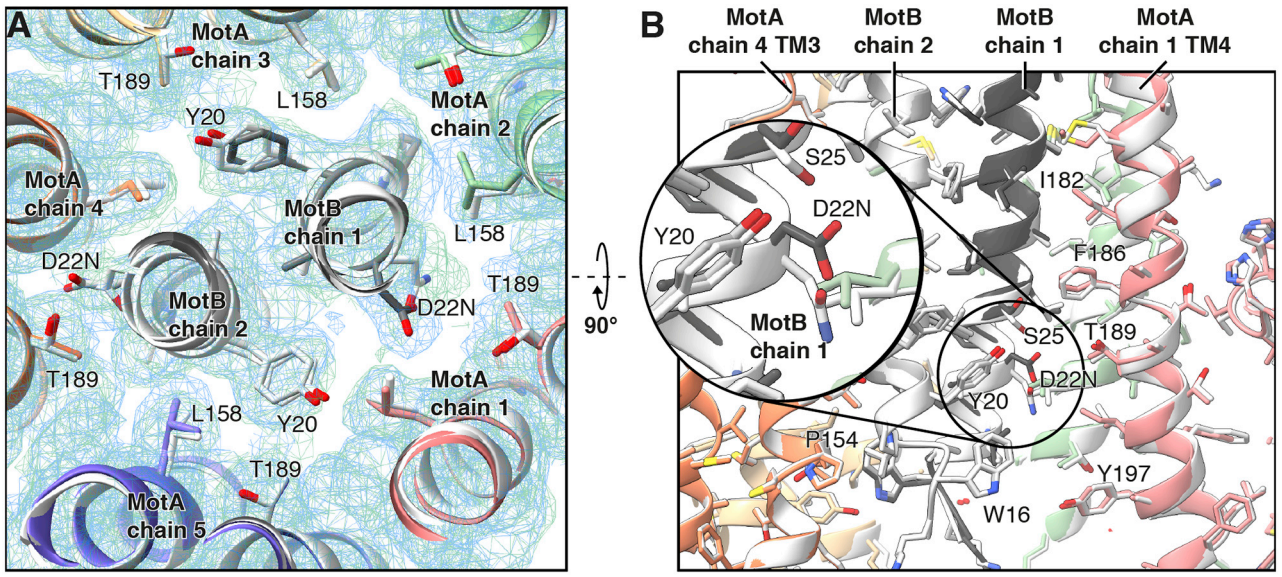

Figure 5. Conformational Changes upon (Mimicking of) (De)protonation

(A) Superposition of *Cj*MotAB(Δ41-60) (light gray) and *Cj*MotAB(Δ41-60, D22N) (same color code as Figure 1) in a closeup view from the periplasmic side. The proton- or hydronium-bound state is mimicked by the mutation D22N. The density maps are shown for both, *Cj*MotAB(Δ41-60) (blue) and *Cj*MotAB(Δ41-60, D22N) (green).

(B) Same as (A) but a side view from within the membrane. The inset shows a magnification of the region around *Cj*MotB chain 1 residue D22/N22, illustrating the conformational change around this residue upon mutation.

See also Figures S4, S5, and S7 and Video S3.

hydrophobic interior of the lipid membrane and therefore rotation of the c-ring (Kühlbrandt and Davies, 2016; Mazhab-Jafari et al., 2016). The protein geometry suggests a CW rotation (when observed from the extracellular/periplasmic side) of MotA around MotB: MotB chain 1 N22 is close to the equivalent position taken up by D22/N22 in MotB chain 2 (near T189), located CW.

The proposed mechanism is very akin to inchworm locomotion. Each MotB D22 alternately engages with MotA, in a site between *Cj*MotA T189, P154, and G150. When MotB D22 is engaged, it can drive a power stroke (when the charge of the other MotB D22 becomes neutralized). When it is not engaged, it picks up a proton from the channel and inches to the position where it can drive the power stroke. The mentioned MotA residues at the site of engagement are extensively conserved across all stator units of rotary prokaryote motors (Baker and Postle, 2013). Furthermore, the *Va*PomA T186A mutation abrogates motility as well as Na^+-dependent structural changes in *Va*PomAB (Onoue et al., 2019), and the corresponding *Se*MotA T209A mutation has a severe motility defect (Figures 3A and 3B), as mentioned (both corresponding to *Cj*MotA T189).

Powering Bidirectional Rotation of the Flagellum

In the following, we present a simple but comprehensive model integrating the data presented here, prior data, and previous models for stator unit activation, torque generation, and directional switching.

Before association with the rotor and peptidoglycan binding, MotAB is in the plugged state and the channel is closed. Association with the rotor and peptidoglycan binding is coupled to unplugging of the channel (Figure 6A). The cytoplasmic domains of MotAB incorporated in the motor are located such that (at least) one of them can interact with FliG $Helix_{Torque}$ (Figure 6B). Based on our structural data, genetic data (Zhou et al., 1998a) and our modeling of the FliG-MotA interaction (Figures S6G and S6H), FliG structural data (Lee et al., 2010), and tomographic data on the *Borrelia burgdorferi* flagellar motor (Chang et al., 2019), the rotor in the CCW state interacts with the inside (the side facing the motor axis) of the stator unit. Upon proton or hydronium binding and release by MotB D22, MotA rotates CW, relative to MotB, which in turn moves the rotor in CCW direction, as MotB is stably anchored to the peptidoglycan. Note that CW rotation of MotA is also predicted by our model outlined in the previous section (Figure 7).

Upon CheY-P-induced directional switching, $FliG_{CC}$ (and therefore FliG $Helix_{Torque}$) makes a ~180° turn relatively to the stator unit (Stock et al., 2012). We propose that the geometry of the stator unit rotor interface allows FliG $Helix_{Torque}$ to now engage the outside (the side facing away from the motor axis) of the MotA pentamer. The rotation of MotA relative to MotB is still the same (CW), but, because of the changed positioning of FliG, the same conformational change in MotA now powers rotation of the rotor in the CW direction (Figure 6B).

The model is consistent with the recently observed structural changes in the C-ring of CCW-biased and CW-locked mutants of *V. alginolyticus* (Carroll et al., 2020) and in the CCW- and CW-locked mutants of *B. burgdorferi* (Chang et al., 2020), where additionally the difference in stator

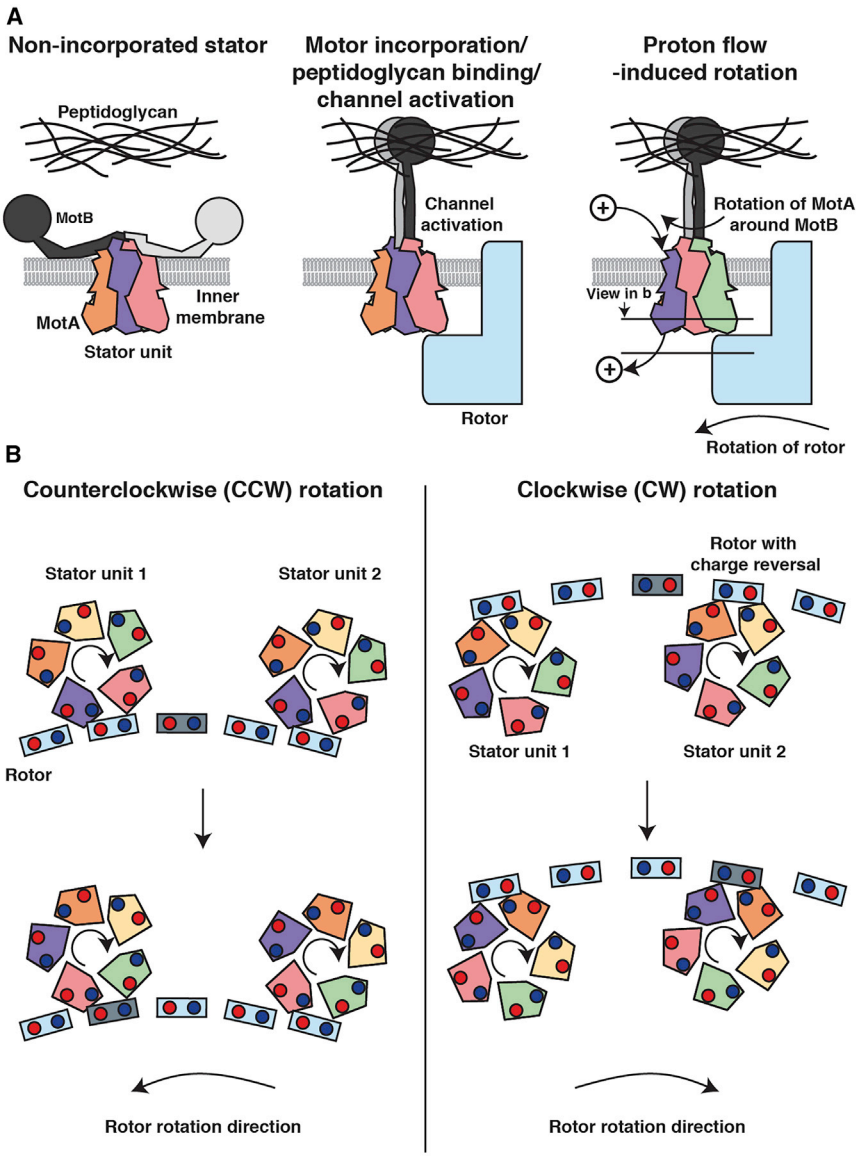

Figure 6. Models of MotAB Activation and Function

(A) Activation mechanism of MotAB. MotB of non-incorporated stator units plugs the proton channel. Motor incorporation is coupled to MotB peptidoglycan binding domain dimerization and peptidoglycan binding. This activates the channel. Proton or hydronium binding and release by the universally conserved MotB aspartate residue (*Cj*MotB D22, *Se*MotB D33) will generate rotation of the MotA pentamer around the MotB dimer, which in turn powers the rotation of the flagellar rotor. MotA and MotB: multi-colored (same color code as Figure 1). A proton or hydronium is represented by a sphere with a + symbol.

(B) Torque generation mechanism during default rotation (CCW, left) and after switching direction (CW, right). Two stator units are shown in top view from the flagellum/extracellular side of the motor. FliG $Helix_{Torque}$ of 5 copies of FliG are shown. MotA: same color code as Figure 1, FliG $Helix_{Torque}$: light blue with 1 copy highlighted in gray blue. Conserved acidic and basic residues (in MotA and FliG $Helix_{Torque}$) are symbolized with red and blue circles, respectively. See Figures S6G and S6H for the modeled MotA–FliG interaction. Rotation directions are given for a motor observed from the extracellular side.

See also Figures S6 and S7 and Videos S4 and S5.

engagement by the C-ring could be observed. Furthermore, the model predicts that the reversal of the ion motive force would invert the rotation direction of the stator unit and hence of the motor. This has previously been observed in *E. coli* (Fung and Berg, 1995), lending experimental support to our model. Moreover, our model does not require any different conformational changes for the stator unit in powering rotation of the rotor in the CCW versus CW directions, consistent with the apparent lack of Che^- mutations in MotA and MotB. According to our model (Figure 7) and the geometry of the rotor and stator unit, binding and release of two protons (two 36° rotations) allows the stator unit to bind the neighboring FliG molecule, or a total of 68 protons per stator unit per rotation of the C-ring (assuming 34 FliG molecules per C-ring), in good agreement with previous estimates (Blair, 2003). The geometry, jointly with the proposed inchworm mechanism of the stator unit, is also consistent with the observed high duty ratio of the motor (Ryu et al., 2000), as the implied handover mechanisms allow that rotor and stator as well as MotA and MotB to remain firmly associated all the time.

In summary, we provide here fundamental insight into stator unit organization and a biophysical model of torque generation and switching of rotational direction of the flagellar motor. These results provide a structure-based framework for a profusion of experiments on stator units of prokaryote rotatory motors, the bacterial flagellar motor, and nanoscale motors in general.

STAR★METHODS

Detailed methods are provided in the online version of this paper and include the following:

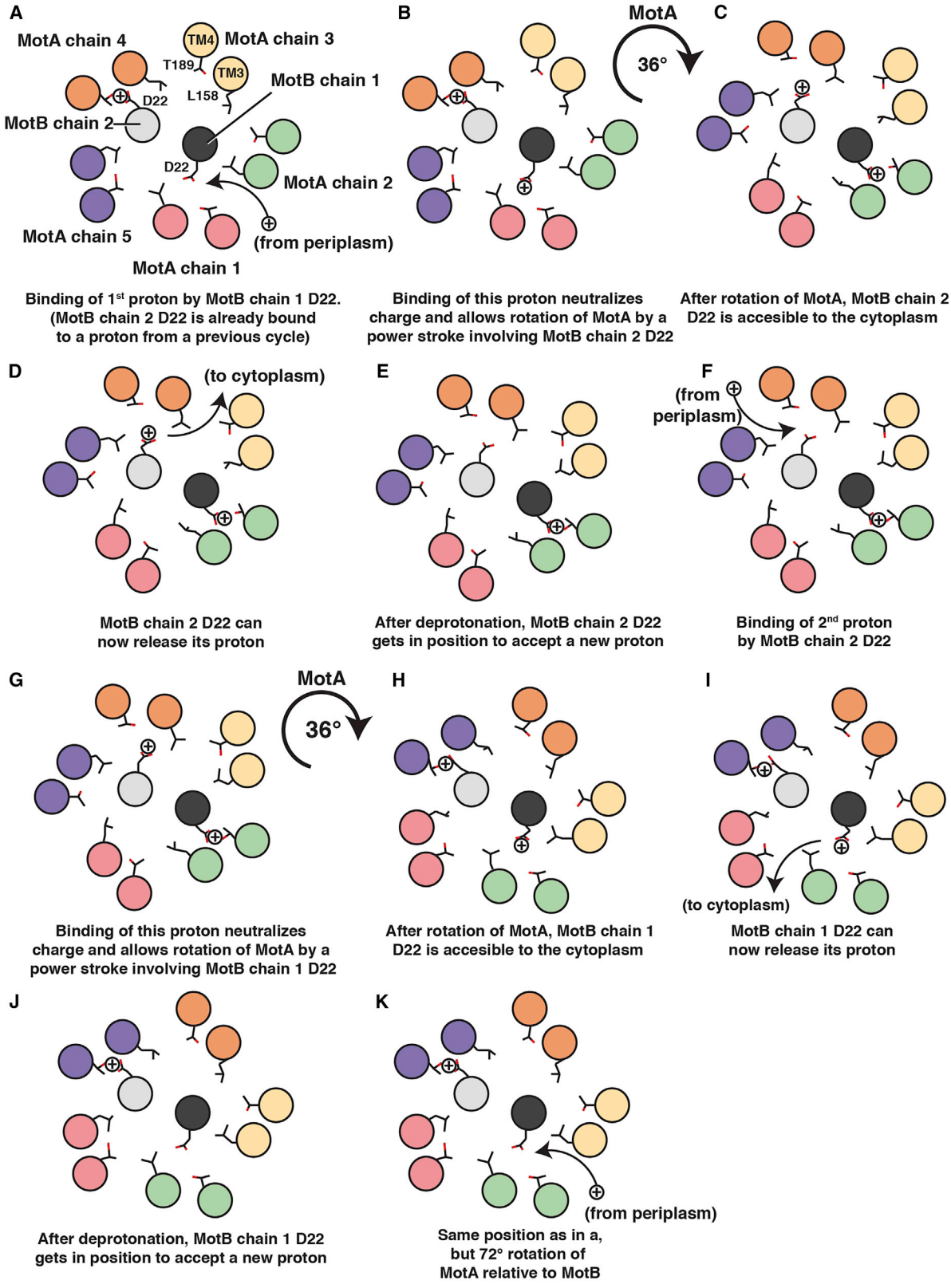

(legend on next page)

SUPPLEMENTAL INFORMATION

Supplemental Information can be found online at https://doi.org/10.1016/j.cell.2020.08.016.

ACKNOWLEDGMENTS

The Novo Nordisk Foundation Center for Protein Research is supported financially by the Novo Nordisk Foundation (NNF14CC0001). This work was also supported by a DFF grant (8123-00002B) and an NNF Hallas-Møller Emerging Investigator grant (NNF17OC0031006) to N.M.I.T., who is also a member of the Integrative Structural Biology Cluster (ISBUC) at the University of Copenhagen. We thank the Danish Cryo-EM Facility at the Core Facility for Integrated Microscopy (CFIM) at the University of Copenhagen and Tillmann Pape for support during data collection. Part of the data processing was performed at the Computerome, the Danish National Computer for Life Sciences. We thank Guillermo Montoya and Carlos Fernández Tornero for feedback on the manuscript.

AUTHOR CONTRIBUTIONS

M.S. cloned, expressed, purified, prepared all cryo-grids, collected cryo-EM data, and determined the structure of *Cj*MotAB (wild type and mutants), *So*-MotAB, and *Va*PomAB. A.R.-E. helped M.S. with protein expression and purification and prepared figures and movies for the manuscript together with N.M.I.T. C.K. generated chromosomal *Se*MotAB mutants and performed and analyzed motility assays and growth curves. C.K. and M.E. interpreted motility and growth curve data and prepared figures for the manuscript. N.M.I.T. planned the experiments, refined and validated the structures, and wrote the first draft of the paper, which was then edited by M.E. and analyzed by N.W., H.C.B., and H.H. All authors contributed to the revision of the manuscript.

DECLARATION OF INTERESTS

The authors declare no competing interests.

Received: May 25, 2020
Revised: July 9, 2020
Accepted: August 11, 2020
Published: September 14, 2020

REFERENCES

Ashkenazy, H., Abadi, S., Martz, E., Chay, O., Mayrose, I., Pupko, T., and Ben-Tal, N. (2016). ConSurf 2016: an improved methodology to estimate and visualize evolutionary conservation in macromolecules. Nucleic Acids Res. *44* (W1), W344–W350.

Baker, K.R., and Postle, K. (2013). Mutations in *Escherichia coli* ExbB transmembrane domains identify scaffolding and signal transduction functions and exclude participation in a proton pathway. J. Bacteriol. *195*, 2898–2911.

Berg, H.C. (2003). The rotary motor of bacterial flagella. Annu. Rev. Biochem. *72*, 19–54.

Berg, H.C., and Anderson, R.A. (1973). Bacteria swim by rotating their flagellar filaments. Nature *245*, 380–382.

Blair, D.F. (2003). Flagellar movement driven by proton translocation. FEBS Lett. *545*, 86–95.

Blair, D.F., and Berg, H.C. (1991). Mutations in the MotA protein of *Escherichia coli* reveal domains critical for proton conduction. J. Mol. Biol. *221*, 1433–1442.

Blair, D.F., Kim, D.Y., and Berg, H.C. (1991). Mutant MotB proteins in *Escherichia coli*. J. Bacteriol. *173*, 4049–4055.

Braun, T.F., and Blair, D.F. (2001). Targeted disulfide cross-linking of the MotB protein of *Escherichia coli*: evidence for two H(+) channels in the stator Complex. Biochemistry *40*, 13051–13059.

Braun, T.F., Al-Mawsawi, L.Q., Kojima, S., and Blair, D.F. (2004). Arrangement of core membrane segments in the MotA/MotB proton-channel complex of Escherichia coli. Biochemistry *43*, 35–45.

Carroll, B.L., Nishikino, T., Guo, W., Zhu, S., Kojima, S., Homma, M., and Liu, J. (2020). The flagellar motor of Vibrio alginolyticus undergoes major structural remodeling during rotational switching. bioRxiv. https://doi.org/10.1101/2020.04.24.060053.

Cascales, E., Lloubès, R., and Sturgis, J.N. (2001). The TolQ-TolR proteins energize TolA and share homologies with the flagellar motor proteins MotA-MotB. Mol. Microbiol. *42*, 795–807.

Celia, H., Noinaj, N., Zakharov, S.D., Bordignon, E., Botos, I., Santamaria, M., Barnard, T.J., Cramer, W.A., Lloubès, R., and Buchanan, S.K. (2016). Structural insight into the role of the Ton complex in energy transduction. Nature *538*, 60–65.

Celia, H., Botos, I., Ni, X., Fox, T., De Val, N., Lloubès, R., Jiang, J., and Buchanan, S.K. (2019). Cryo-EM structure of the bacterial Ton motor subcomplex ExbB-ExbD provides information on structure and stoichiometry. Commun. Biol. *358*. Published online October 4, 2019. https://doi.org/10.1038/s42003-019-0604-2.

Figure 7. Mechanistic Model for Proton Motive Force-Powered Rotation of MotA around MotB

(A) MotB chain 1 D22 binds a proton (or hydronium, represented by a sphere with a + symbol) from the periplasmic side.
(B) Proton (or hydronium) binding neutralizes charge and MotA rotates 36° clockwise (CW) by a power stroke involving MotB chain 2 D22.
(C and D) (C) Now, the MotB chain 2 D22 is accessible to the cytoplasm. (D) MotB chain 2 D22 releases its proton.
(E and F) (E) After deprotonation, the MotB chain 2 D22 gets in position. (F) MotB chain 2 D22 binds a new proton.
(G) As before, binding of this proton neutralizes charge, which allows 36° rotation of MotA by a power stroke involving MotB chain 1 D22.
(H and I) (H) MotB chain 1 D22 is accessible to the cytoplasm. (I) MotB chain 1 D22 can now release its proton.
(J) After deprotonation, MotB chain 1 D22 gets in position to accept a new proton.
(K) Same as in (A) but after a 72° rotation of MotA relative to MotB.
See also Videos S4 and S5.

Chang, Y., Moon, K.H., Zhao, X., Norris, S.J., Motaleb, M.A., and Liu, J. (2019). Structural insights into flagellar stator-rotor interactions. eLife *8*, 147.

Chang, Y., Zhang, K., Carroll, B., Zhao, X., Charon, N.W., Norris, S.J., Motaleb, M.A., Li, C., and Liu, J. (2020). Molecular mechanism for rotational switching of the bacterial flagellar motor. bioRxiv. https://doi.org/10.1101/2020.05.18.101634.

Chen, S., McMullan, G., Faruqi, A.R., Murshudov, G.N., Short, J.M., Scheres, S.H.W., and Henderson, R. (2013). High-resolution noise substitution to measure overfitting and validate resolution in 3D structure determination by single particle electron cryomicroscopy. Ultramicroscopy *135*, 24–35.

Chorev, D.S., Baker, L.A., Wu, D., Beilsten-Edmands, V., Rouse, S.L., Zeev-Ben-Mordehai, T., Jiko, C., Samsudin, F., Gerle, C., Khalid, S., et al. (2018). Protein assemblies ejected directly from native membranes yield complexes for mass spectrometry. Science *362*, 829–834.

Coulton, J.W., and Murray, R.G. (1978). Cell envelope associations of *Aquaspirillum serpens* flagella. J. Bacteriol. *136*, 1037–1049.

Datsenko, K.A., and Wanner, B.L. (2000). One-step inactivation of chromosomal genes in Escherichia coli K-12 using PCR products. Proc. Natl. Acad. Sci. USA *97*, 6640–6645. https://doi.org/10.1073/pnas.120163297.

Dean, G.E., Macnab, R.M., Stader, J., Matsumura, P., and Burks, C. (1984). Gene sequence and predicted amino acid sequence of the motA protein, a membrane-associated protein required for flagellar rotation in *Escherichia coli*. J. Bacteriol. *159*, 991–999.

DeRosier, D.J. (1998). The turn of the screw: the bacterial flagellar motor. Cell *93*, 17–20.

Duan, Q., Zhou, M., Zhu, L., and Zhu, G. (2013). Flagella and bacterial pathogenicity. J. Basic Microbiol. *53*, 1–8.

Emsley, P., Lohkamp, B., Scott, W.G., and Cowtan, K. (2010). Features and development of Coot. Acta Crystallogr. D Biol. Crystallogr. *66*, 486–501.

Evans, L.D.B., Hughes, C., and Fraser, G.M. (2014). Building a flagellum outside the bacterial cell. Trends Microbiol. *22*, 566–572.

Fung, D.C., and Berg, H.C. (1995). Powering the flagellar motor of *Escherichia coli* with an external voltage source. Nature *375*, 809–812.

Goddard, T.D., Huang, C.C., Meng, E.C., Pettersen, E.F., Couch, G.S., Morris, J.H., and Ferrin, T.E. (2018). UCSF ChimeraX: Meeting modern challenges in visualization and analysis. Protein Sci. *27*, 14–25.

Grant, T., Rohou, A., and Grigorieff, N. (2018). *cis*TEM, user-friendly software for single-particle image processing. eLife *7*, e35383.

Haiko, J., and Westerlund-Wikström, B. (2013). The role of the bacterial flagellum in adhesion and virulence. Biology (Basel) *2*, 1242–1267.

Hall, B.G., Acar, H., Nandipati, A., and Barlow, M. (2014). Growth rates made easy. Mol. Biol. Evol. *31*, 232–238.

Hirota, N., and Imae, Y. (1983). Na+-driven flagellar motors of an alkalophilic *Bacillus* strain YN-1. J. Biol. Chem. *258*, 10577–10581.

Hosking, E.R., Vogt, C., Bakker, E.P., and Manson, M.D. (2006). The *Escherichia coli* MotAB proton channel unplugged. J. Mol. Biol. *364*, 921–937.

Jurrus, E., Engel, D., Star, K., Monson, K., Brandi, J., Felberg, L.E., Brookes, D.H., Wilson, L., Chen, J., Liles, K., et al. (2018). Improvements to the APBS biomolecular solvation software suite. Protein Sci. *27*, 112–128.

Karlinsey, J.E. (2007). lambda-Red genetic engineering in *Salmonella enterica* serovar Typhimurium. Methods Enzymol. *421*, 199–209.

Khan, S., Dapice, M., and Reese, T.S. (1988). Effects of mot gene expression on the structure of the flagellar motor. J. Mol. Biol. *202*, 575–584.

Khan, S., Khan, I.H., and Reese, T.S. (1991). New structural features of the flagellar base in *Salmonella typhimurium* revealed by rapid-freeze electron microscopy. J. Bacteriol. *173*, 2888–2896.

Khan, S., Ivey, D.M., and Krulwich, T.A. (1992). Membrane ultrastructure of alkaliphilic *Bacillus* species studied by rapid-freeze electron microscopy. J. Bacteriol. *174*, 5123–5126.

Kojima, S., and Blair, D.F. (2001). Conformational change in the stator of the bacterial flagellar motor. Biochemistry *40*, 13041–13050.

Kojima, S., and Blair, D.F. (2004). Solubilization and purification of the MotA/MotB complex of *Escherichia coli*. Biochemistry *43*, 26–34.

Kojima, S., Takao, M., Almira, G., Kawahara, I., Sakuma, M., Homma, M., Kojima, C., and Imada, K. (2018). The helix rearrangement in the periplasmic domain of the flagellar stator B subunit activates peptidoglycan binding and ion influx. Structure *26*, 590–598.

Kühlbrandt, W., and Davies, K.M. (2016). Rotary ATPases: A new twist to an ancient machine. Trends Biochem. Sci. *41*, 106–116.

Lai, Y.-W., Ridone, P., Peralta, G., Tanaka, M.M., and Baker, M.A.B. (2020). Evolution of the stator elements of rotary prokaryote motors. J. Bacteriol. *202*, e00557, e19.

Lam, K.-H., Ip, W.-S., Lam, Y.-W., Chan, S.-O., Ling, T.K.-W., and Au, S.W.-N. (2012). Multiple conformations of the FliG C-terminal domain provide insight into flagellar motor switching. Structure *20*, 315–325.

Larsen, S.H., Adler, J., Gargus, J.J., and Hogg, R.W. (1974). Chemomechanical coupling without ATP: the source of energy for motility and chemotaxis in bacteria. Proc. Natl. Acad. Sci. USA *71*, 1239–1243.

Lee, L.K., Ginsburg, M.A., Crovace, C., Donohoe, M., and Stock, D. (2010). Structure of the torque ring of the flagellar motor and the molecular basis for rotational switching. Nature *466*, 996–1000.

Liebschner, D., Afonine, P.V., Baker, M.L., Bunkóczi, G., Chen, V.B., Croll, T.I., Hintze, B., Hung, L.-W., Jain, S., McCoy, A.J., et al. (2019). Macromolecular structure determination using X-rays, neutrons and electrons: recent developments in Phenix. Acta Crystallogr. D Struct. Biol. *75*, 861–877.

Lo, C.-J., Sowa, Y., Pilizota, T., and Berry, R.M. (2013). Mechanism and kinetics of a sodium-driven bacterial flagellar motor. Proc. Natl. Acad. Sci. USA *110*, E2544–E2551.

London, N., Raveh, B., Cohen, E., Fathi, G., and Schueler-Furman, O. (2011). Rosetta FlexPepDock web server–high resolution modeling of peptide-protein interactions. Nucleic Acids Res. *39*, W249-53.

Ma, P., Varela, F., Magoch, M., Silva, A.R., Rosário, A.L., Brito, J., Oliveira, T.F., Nogly, P., Pessanha, M., Stelter, M., et al. (2013). An efficient strategy for small-scale screening and production of archaeal membrane transport proteins in Escherichia coli. PLoS ONE *8*, e76913.

Maki-Yonekura, S., Matsuoka, R., Yamashita, Y., Shimizu, H., Tanaka, M., Iwabuki, F., and Yonekura, K. (2018). Hexameric and pentameric complexes of the ExbBD energizer in the Ton system. eLife *7*, e35419.

Mandadapu, K.K., Nirody, J.A., Berry, R.M., and Oster, G. (2015). Mechanics of torque generation in the bacterial flagellar motor. Proc. Natl. Acad. Sci. USA *112*, E4381–E4389.

Mazhab-Jafari, M.T., Rohou, A., Schmidt, C., Bueler, S.A., Benlekbir, S., Robinson, C.V., and Rubinstein, J.L. (2016). Atomic model for the membrane-embedded V_O motor of a eukaryotic V-ATPase. Nature *539*, 118–122.

Minamino, T., Kinoshita, M., and Namba, K. (2019). Directional Switching Mechanism of the Bacterial Flagellar Motor. Comput. Struct. Biotechnol. J. *17*, 1075–1081.

Morimoto, Y.V., and Minamino, T. (2014). Structure and function of the bi-directional bacterial flagellar motor. Biomolecules *4*, 217–234.

Morimoto, Y.V., Che, Y.-S., Minamino, T., and Namba, K. (2010). Proton-conductivity assay of plugged and unplugged MotA/B proton channel by cytoplasmic pHluorin expressed in *Salmonella*. FEBS Lett. *584*, 1268–1272.

Nakamura, S., and Minamino, T. (2019). Flagella-driven motility of bacteria. Biomolecules *9*, 279.

Onoue, Y., Iwaki, M., Shinobu, A., Nishihara, Y., Iwatsuki, H., Terashima, H., Kitao, A., Kandori, H., and Homma, M. (2019). Essential ion binding residues for Na^+ flow in stator complex of the Vibrio flagellar motor. Sci. Rep. *9*, 11216.

Pettersen, E.F., Goddard, T.D., Huang, C.C., Couch, G.S., Greenblatt, D.M., Meng, E.C., and Ferrin, T.E. (2004). UCSF Chimera–a visualization system for exploratory research and analysis. J. Comput. Chem. *25*, 1605–1612.

Pravda, L., Sehnal, D., Toušek, D., Navrátilová, V., Bazgier, V., Berka, K., Svobodová Vareková, R., Koca, J., and Otyepka, M. (2018). MOLEonline: a

web-based tool for analyzing channels, tunnels and pores (2018 update). Nucleic Acids Res. *46* (W1), W368–W373.

Punjani, A., Rubinstein, J.L., Fleet, D.J., and Brubaker, M.A. (2017). cryoSPARC: algorithms for rapid unsupervised cryo-EM structure determination. Nat. Methods *14*, 290–296.

Raveh, B., London, N., and Schueler-Furman, O. (2010). Sub-angstrom modeling of complexes between flexible peptides and globular proteins. Proteins *78*, 2029–2040.

Rohou, A., and Grigorieff, N. (2015). CTFFIND4: Fast and accurate defocus estimation from electron micrographs. J. Struct. Biol. *192*, 216–221.

Roujeinikova, A. (2008). Crystal structure of the cell wall anchor domain of MotB, a stator component of the bacterial flagellar motor: implications for peptidoglycan recognition. Proc. Natl. Acad. Sci. USA *105*, 10348–10353.

Ryu, W.S., Berry, R.M., and Berg, H.C. (2000). Torque-generating units of the flagellar motor of *Escherichia coli* have a high duty ratio. Nature *403*, 444–447.

Sakai, T., Miyata, T., Terahara, N., Mori, K., Inoue, Y., Morimoto, Y.V., Kato, T., Namba, K., and Minamino, T. (2019). Novel insights into conformational rearrangements of the bacterial flagellar switch complex. MBio *10*, 19.

Sali, A., and Blundell, T.L. (1993). Comparative protein modelling by satisfaction of spatial restraints. J. Mol. Biol. *234*, 779–815.

Sato, K., and Homma, M. (2000). Multimeric structure of PomA, a component of the Na+-driven polar flagellar motor of *vibrio alginolyticus*. J. Biol. Chem. *275*, 20223–20228.

Schneider, C.A., Rasband, W.S., and Eliceiri, K.W. (2012). NIH Image to ImageJ: 25 years of image analysis. Nat. Methods *9*, 671–675.

Sharp, L.L., Zhou, J., and Blair, D.F. (1995a). Features of MotA proton channel structure revealed by tryptophan-scanning mutagenesis. Proc. Natl. Acad. Sci. USA *92*, 7946–7950.

Sharp, L.L., Zhou, J., and Blair, D.F. (1995b). Tryptophan-scanning mutagenesis of MotB, an integral membrane protein essential for flagellar rotation in *Escherichia coli*. Biochemistry *34*, 9166–9171.

Silverman, M., and Simon, M. (1974). Flagellar rotation and the mechanism of bacterial motility. Nature *249*, 73–74.

Stader, J., Matsumura, P., Vacante, D., Dean, G.E., and Macnab, R.M. (1986). Nucleotide sequence of the *Escherichia coli* motB gene and site-limited incorporation of its product into the cytoplasmic membrane. J. Bacteriol. *166*, 244–252.

Stock, D., Namba, K., and Lee, L.K. (2012). Nanorotors and self-assembling macromolecular machines: the torque ring of the bacterial flagellar motor. Curr. Opin. Biotechnol. *23*, 545–554.

Sudo, Y., Terashima, H., Abe-Yoshizumi, R., Kojima, S., and Homma, M. (2009). Comparative study of the ion flux pathway in stator units of proton- and sodium-driven flagellar motors. Biophysics (Nagoya-Shi) *5*, 45–52.

Sun, M., Wartel, M., Cascales, E., Shaevitz, J.W., and Mignot, T. (2011). Motor-driven intracellular transport powers bacterial gliding motility. Proc. Natl. Acad. Sci. USA *108*, 7559–7564.

Suzuki, Y., Morimoto, Y.V., Oono, K., Hayashi, F., Oosawa, K., Kudo, S., and Nakamura, S. (2019). Effect of the MotA(M206I) Mutation on torque generation and stator assembly in the *Salmonella* H+-driven flagellar motor. J. Bacteriol. *201*, 19.

Sverzhinsky, A., Chung, J.W., Deme, J.C., Fabre, L., Levey, K.T., Plesa, M., Carter, D.M., Lypaczewski, P., and Coulton, J.W. (2015). Membrane protein complex ExbB4-ExbD1-TonB1 from *Escherichia coli* demonstrates conformational plasticity. J. Bacteriol. *197*, 1873–1885.

Takekawa, N., Terahara, N., Kato, T., Gohara, M., Mayanagi, K., Hijikata, A., Onoue, Y., Kojima, S., Shirai, T., Namba, K., and Homma, M. (2016). The tetrameric MotA complex as the core of the flagellar motor stator from hyperthermophilic bacterium. Sci. Rep. *6*, 31526.

Tan, Y.Z., Baldwin, P.R., Davis, J.H., Williamson, J.R., Potter, C.S., Carragher, B., and Lyumkis, D. (2017). Addressing preferred specimen orientation in single-particle cryo-EM through tilting. Nat. Methods *14*, 793–796.

Tang, H., Braun, T.F., and Blair, D.F. (1996). Motility protein complexes in the bacterial flagellar motor. J. Mol. Biol. *261*, 209–221.

Terauchi, T., Terashima, H., Kojima, S., and Homma, M. (2011). A conserved residue, PomB-F22, in the transmembrane segment of the flagellar stator complex, has a critical role in conducting ions and generating torque. Microbiology *157*, 2422–2432.

Williams, C.J., Headd, J.J., Moriarty, N.W., Prisant, M.G., Videau, L.L., Deis, L.N., Verma, V., Keedy, D.A., Hintze, B.J., Chen, V.B., et al. (2018). MolProbity: More and better reference data for improved all-atom structure validation. Protein Sci. *27*, 293–315.

Wilson, M.L., and Macnab, R.M. (1988). Overproduction of the MotA protein of *Escherichia coli* and estimation of its wild-type level. J. Bacteriol. *170*, 588–597.

Yamaguchi, S., Fujita, H., Ishihara, A., Aizawa, S., and Macnab, R.M. (1986). Subdivision of flagellar genes of *Salmonella typhimurium* into regions responsible for assembly, rotation, and switching. J. Bacteriol. *166*, 187–193.

Yonekura, K., Maki-Yonekura, S., and Homma, M. (2011). Structure of the flagellar motor protein complex PomAB: implications for the torque-generating conformation. J. Bacteriol. *193*, 3863–3870.

Zheng, S.Q., Palovcak, E., Armache, J.-P., Verba, K.A., Cheng, Y., and Agard, D.A. (2017). MotionCor2: anisotropic correction of beam-induced motion for improved cryo-electron microscopy. Nat. Methods *14*, 331–332.

Zhou, J., and Blair, D.F. (1997). Residues of the cytoplasmic domain of MotA essential for torque generation in the bacterial flagellar motor. J. Mol. Biol. *273*, 428–439.

Zhou, J., Fazzio, R.T., and Blair, D.F. (1995). Membrane topology of the MotA protein of *Escherichia coli*. J. Mol. Biol. *251*, 237–242.

Zhou, J., Lloyd, S.A., and Blair, D.F. (1998a). Electrostatic interactions between rotor and stator in the bacterial flagellar motor. Proc. Natl. Acad. Sci. USA *95*, 6436–6441.

Zhou, J., Sharp, L.L., Tang, H.L., Lloyd, S.A., Billings, S., Braun, T.F., and Blair, D.F. (1998b). Function of protonatable residues in the flagellar motor of *Escherichia coli*: a critical role for Asp 32 of MotB. J. Bacteriol. *180*, 2729–2735.

Zivanov, J., Nakane, T., Forsberg, B.O., Kimanius, D., Hagen, W.J., Lindahl, E., and Scheres, S.H. (2018). New tools for automated high-resolution cryo-EM structure determination in RELION-3. eLife *7*, 163.

STAR★METHODS

KEY RESOURCES TABLE

REAGENT or RESOURCE	SOURCE	IDENTIFIER
Bacterial and Virus Strains		
Escherichia coli C43(DE3)	LuBioScience GmbH	Cat # 60446-1
Campylobacter jejuni	ATCC	ATCC BAA-2151
Shewanella oneidensis	ATCC	ATCC 700550
Vibrio alginolyticus	DSMZ	ATCC 17749
Salmonella enterica subsp. *enterica* serovar Typhimurium LT2	ATCC	ATCC 700720
All *Se*MotAB amino acid point mutant strains, see Table S2	This paper	N/A
Chemicals, Peptides, and Recombinant Proteins		
Lauryl Maltose Neopentyl Glycol (LMNG)	Anatrace	Cat # NG310
Strep-Tactin Superfrow high capacity	IBA	Cat # 2-1208-002
Superose 6, XK 16/70	GE Healthcare	N/A
S7 Phusion Polymerase	Mobidiag	Cat # MB-S7-100
*Cj*MotAB	This paper	N/A
*Cj*MotAB(Δ41-60)	This paper	N/A
*Cj*MotAB(Δ41-60, D22N)	This paper	N/A
*So*MotAB	This paper	N/A
*Va*PomAB	This paper	N/A
Critical Commercial Assays		
SuperFi PCR Master Mix	Invitrogen	Cat # 12358250
NEBuilder HiFi DNA Assembly Master Mix	New England Biolabs	Cat # E2621L
Deposited Data		
Coordinates and Cryo-EM map of *Cj*MotAB	This paper	PDB: 6YKM EMDB: EMD-10828
Coordinates and Cryo-EM map of *Cj*MotAB(Δ41-60)	This paper	PDB: 6YKP EMDB: EMD-10829
Coordinates and Cryo-EM map of *Cj*MotAB(Δ41-60, D22N)	This paper	PDB: 6YKR EMDB: EMD-10830
Cryo-EM map of *So*MotAB	This paper	EMDB: EMD-10831
Cryo-EM map of *Va*PomAB	This paper	EMDB: EMD-10832
Oligonucleotides		
Primers for cloning and mutagenesis, see Table S3	This paper	N/A
Recombinant DNA		
pET11a C-3C-TwinStrepII	This paper	pNTL075
pET11a CjMotA-CjMotB-3C-TwinStrepII	This paper	pNTL109
pET11a CjMotA-CjMotB(Δ41-60)-3C-TwinStrepII	This paper	pNTL147
pET11a CjMotA-CjMotB(Δ41-60, D22N)-3C-TwinStrepII	This paper	pNTL148
pET11a SoMotA-SoMotB-3C-TwinStrepII	This paper	pNTL110
pET11a VaPomA-VaPomB-3C-TwinStrepII	This paper	pNTL079
pET11a SeMotA-SeMotB-3C-TwinStrepII	This paper	pNTL135
All *Se*MotAB amino acid point mutations in: pET11a SeMotA-SeMotB-3C-TwinStrepII	This paper	GenScript
pKD46 (lambda-Red recombinase plasmid)	Datsenko and Wanner, 2000	N/A
Software and Algorithms		
RELION 3.0	Zivanov et al., 2018	https://www3.mrc-lmb.cam.ac.uk/relion/
cryoSPARC and cryoSPARC Live	Punjani et al., 2017	https://cryosparc.com/
cisTEM	Grant et al., 2018	https://cistem.org/

(*Continued on next page*)

Continued

REAGENT or RESOURCE	SOURCE	IDENTIFIER
MotionCor2	Zheng et al., 2017	https://msg.ucsf.edu/
CTFFIND-4.1	Rohou and Grigorieff, 2015	https://grigoriefflab.umassmed.edu/
Remote 3DFSC Processing Server	Tan et al., 2017	https://3dfsc.salk.edu/
Coot	Emsley et al., 2010	https://www2.mrc-lmb.cam.ac.uk/personal/pemsley/coot/
PHENIX	Liebschner et al., 2019	https://www.phenix-online.org/
MolProbity	Williams et al., 2018	http://molprobity.biochem.duke.edu/
Modeler	Sali and Blundell, 1993	https://salilab.org/modeller/
Mole 2.5	Pravda et al., 2018	https://webchem.ncbr.muni.cz/Platform/App/Mole
UCSF Chimera	Pettersen et al., 2004	https://www.cgl.ucsf.edu/chimera/
UCSF ChimeraX	Goddard et al., 2018	https://www.cgl.ucsf.edu/chimerax/
ImageJ 2.0.0	Schneider et al., 2012	https://imagej.nih.gov/ij/
GrowthRates 4.3	Hall et al., 2014	https://sourceforge.net/projects/growthrates/
GraphPad Prism 8	GraphPad Software	N/A
Illustrator	Adobe	N/A
Premiere Pro	Adobe	N/A
Keynote	Apple	N/A
Other		
Grids Quantifoil R2/1 300 mesh Cu	Plano GmbH	Cat # S174-2

RESOURCE AVAILABILITY

Lead Contact

Further information and requests for resources and reagents should be directed to and will be fulfilled by the Lead Contact, Nicholas M. I. Taylor (nicholas.taylor@cpr.ku.dk).

Materials Availability

Plasmids generated in this study are available upon request.

Data and Code Availability

Atomic coordinates for *Cj*MotAB, *Cj*MotAB(Δ41-60), and *Cj*MotAB(Δ41-60, D22N) were deposited in the Protein Data Bank under accession codes PDB: 6YKM, 6YKP, and 6YKR, respectively. The corresponding electrostatic potential maps were deposited in the Electron Microscopy Data Bank (EMDB) under accession codes EMDB: EMD-10828, EMD-10829, and EMD-10830, respectively. The electrostatic potential maps for *So*MotAB and *Va*PomAB were deposited in the EMDB under accession codes EMDB: EMD-10831 and EMD-10832, respectively.

EXPERIMENTAL MODEL AND SUBJECT DETAILS

Bacterial strains and culture conditions

E. coli Overexpress™ C43(DE3) used for protein purification was cultured in LB medium supplemented with ampicillin (100 μg/ml) first at 37°C (growing phase) and later 30°C (protein expression). *Salmonella enterica* serovar Typhimurium LT2 (wild-type and mutants) used for motility assays was grown in LB medium at 37°C. Swimming motility was determined using tryptone broth (TB)-based soft agar plates containing 0.3% agar, inoculated with the overnight cultures and incubated at 37°C.

METHOD DETAILS

Cloning, expression and purification

The *Cj*MotAB fragment was amplified from *Campylobacter jejuni* (ATCC BAA-2151), *So*MotAB from *Shewanella oneidensis* (ATCC 700550) and *Va*PomAB from *Vibrio alginolyticus* (ATCC 17749). They were all cloned into a modified pET vector containing a C-terminal human rhinovirus (HRV) 3C protease cleavage site and a twin-Strep-tag II (resulting in pET11a-MotA-MotB-3C-TSII). All complexes were expressed in *E. coli* Overexpress™ C43(DE3) cells (LuBioScience GmbH) adapting published protocols (Ma

et al., 2013). Briefly, cells were cultured in 2 l LB medium (supplemented with 100 μg/ml ampicillin) at 37°C and protein expression was induced with 0.5 mM IPTG at OD_{600} 0.4−0.8. Cells were incubated for another 3 hours at 30°C and then harvested. The cell pellet was resuspended in 50 mL 200 mM Tris-HCl pH 8.0 and incubated at room temperature for 20 min with shaking. To gently disrupt the cells, 24.3 mL of 200 mM Tris-HCl pH 8.0 containing 1 M sucrose and 1 mM EDTA was added first, followed by addition of 330 μl 10 mg/ml lysozyme and 48 mL deionized water. After 20 min shaking at room temperature, spheroplasts were sedimented at 18,000 × *g* for 30 min. The pellet was resuspended in 100 mL 10 mM Tris-HCl pH 8.0 and incubated at room temperature for 30 min while stirring. DNase I was added to improve pellet solubilization. Membranes were then sedimented at 18,000 × *g* for 30 min, resuspended in a buffer containing 10 mM Tris-HCl pH 8.0 and 5% glycerol and stored at −80°C.

Membranes were solubilized in 1% (w:v) Lauryl Maltose Neopentyl Glycol (LMNG) (Anatrace) for 2 hours shaking on a rocking platform and then ultracentrifuged for 30 min at 100,000 × *g*. The supernatant was added to a gravity flow column containing 2 mL of Strep beads (IBA), pre-equilibrated with wash buffer (20 mM Tris-HCl pH 8.0, 150 mM NaCl, 20% glycerol and 0.005% LMNG). Beads were washed five times with 2 column volumes of wash buffer and elution was performed six times with 0.5 column volumes of elution buffer (20 mM Tris-HCl pH 8.0, 150 mM NaCl, 20% glycerol, 0.005% LMNG and 10 mM desthiobiotin).

The protein complex was then loaded onto a Superose 6, XK 16/70 gel filtration column (GE Healthcare), which was pre-equilibrated with 20 mM Tris-HCl pH 8, 150 mM NaCl and 0.002% LMNG. The peak fractions corresponding to the protein complex were concentrated to about 0.6 mg/ml using a centrifugal filter with a PES membrane (Sartorius) and used for preparation of cryo-EM sample grids.

Sample preparation and cryo-EM data collection

3 μl of freshly purified sample was applied onto glow-discharged (30 s, 0.15 mbar) (Balzers Union dual chamber CTA 010 glow discharger) grids (Quantifoil R2/1 300 mesh Cu) and plunge-frozen into liquid ethane using a Vitrobot Mark IV (FEI, Thermo Fisher Scientific). The settings were as follows: 4°C, 100% humidity, 7 s wait time, 3 s blot time, and a blot force of 0. Movies were collected using the semi-automated acquisition program EPU (FEI, Thermo Fisher Scientific) on a Titan Krios G2 microscope operated at 300 keV paired with a Falcon 3EC direct electron detector (FEI, Thermo Fisher Scientific). Images were recorded in electron counting mode, at 96,000x magnification with a calibrated pixel size of 0.832 Å and underfocus range of 1 to 3 μm. Number of micrographs and total exposure values for the different datasets are summarized in Table S1.

Image processing

Image processing of the *Cj*MotAB, *Cj*MotAB(Δ41-60, D22N) and *Va*PomAB datasets was performed using RELION 3.0 (Zivanov et al., 2018) (Figures S2 and S4). Micrographs were aligned and dose-weighted using MotionCor2 (Zheng et al., 2017) and the contrast transfer function (CTF) was estimated using CTFFIND-4.1 (Rohou and Grigorieff, 2015). The *Cj*MotAB(Δ41-60) and *So*MotAB datasets were processed in cryoSPARC Live and cryoSPARC (Punjani et al., 2017), respectively (Figure S3). In this case, Patch motion correction and Patch CTF estimation were performed instead.

To make a 2D template for picking, a first particle picking job was done on a random subset of around 1,000 micrographs, using Laplacian-of-Gaussian picking (RELION) or blob picker (cryoSPARC Live and cryoSPARC). Selected 2D class averages were used as templates for reference-based automated particle picking from all the micrographs. Picked particles were extracted using a box size of 64 pixels (256 pixels binned 4 times). After an initial sorting and at least 4 rounds of 2D classification, selected particles were re-extracted to a box size of 256 pixels and a 3D model was created *de novo*. This initial model was low-pass filtered to 60 Å and used in a 3D classification of the particles. The best class or classes were further processed in a 3D high-resolution refinement job. In cryoSPARC the map was sharpened during the same job using a dynamic mask, while in RELION mask creation and postprocessing jobs were performed to sharpen the maps by applying a B-factor corrected for the modulation transfer function of the detector. Finally, in RELION particles were further processed using per-particle CTF refinement and Bayesian polishing (including beam tilt estimation). Local resolution estimations were also obtained within RELION.

This general approach had to be modified for the *So*MotAB and *Va*PomAB datasets. Due to the preferential orientation *So*MotAB, further 3D classification jobs were performed, together with 2D classification jobs in order to keep as many side views as possible. In the case of *Va*PomAB, the initial model had to be generated with cisTEM (Grant et al., 2018).

Directional resolution anisotropy, which is caused by preferential orientation, was assessed using the Remote 3DFSC Processing Server (Tan et al., 2017) (https://3dfsc.salk.edu/). The number of picked and final particles, map-sharpening B-factor and final map resolution values for all datasets can be found in Table S1.

Global FSC curves shown in the figures have been corrected for the effects of masking (Chen et al., 2013).

Atomic model building, refinement and validation

De novo model building was performed manually using Coot (Emsley et al., 2010). Models were refined using PHENIX (Liebschner et al., 2019) real space refinement. The geometry of the structures was validated using MolProbity (Williams et al., 2018) (Table S1). Despite trying extensively, unlike for the *Cj*MotAB and *Cj*MotAB(Δ41-60, D22N) structures, it was impossible to fit a regular α-helix in the density around *Cj*MotAB(Δ41-60) MotB chain 1 D22 while respecting the chirality of this residue. The structure does fit very well to the map when introducing cis-peptides before and after this residue, which also point the carbonyl oxygen atoms to chemically plausible directions. We further validated the atomic model of *Cj*MotAB by plotting existing biological data obtained for *E. coli* MotAB from

cross-linking experiments (Braun et al., 2004), mutational screening (Blair and Berg, 1991; Blair et al., 1991) or tryptophan scanning analysis (Sharp et al., 1995a, b) on the structure. Only residues above an alignment score cutoff of 2 (out of 11) for the alignment were plotted.

Homology modeling of SeMotAB, modeling the MotA–FliG interaction and ion channel prediction

*Se*MotAB was modeled based on the structure of *Cj*MotAB with Modeler (Sali and Blundell, 1993). The alignment (Figure S1) between *Cj*MotA and *Se*MotA, and between *Cj*MotB and *Se*MotB, respectively, was provided to model the complete *Se*MotAB heteroheptamer. Non-conserved regions (*Se*MotA 107-123 and 279-295) were removed for displaying.

C. jejuni FliG (*Cj*FliG residues 115-334) was modeled based on the structure of *H. pylori* $FliG_{MC1}$ (Lam et al., 2012) (PDB: 3USW). The $FliG\ Helix_{Torque}$ peptide (*Cj*FliG residues 290-305) was extracted from this model for the following. Two subunits of MotA were extracted from the *Cj*MotAB atomic model generated in the present study and linked together from the C-terminal end of one to the N-terminal end of the other to allow submission to the FlexPepDock server (London et al., 2011; Raveh et al., 2010). The peptide was located in different positions, either on top of one MotA or in between two MotA subunits trying to maximize interaction between genetically interacting, oppositely charged residues (as described [Zhou et al., 1998a]) and uploaded to the server. The best docking results, which corresponded to $FliG\ Helix_{Torque}$ interacting in between MotA monomers and also correlated with the electrostatic interaction data, were later manually readjusted in terms of rotamers, distances and position of the peptide. The process of submission and selection was repeated and the result with the best score (total: 5,981.675, rmsBB: 2.320) was chosen for plotting and analysis.

For calculation of a proton and hydronium accessible channel, the *Cj*MotAB(Δ41-60) model was analyzed using Mole 2.5 software (Pravda et al., 2018). The bottleneck radius was set to 1 Å. The starting points for calculation were located along the interface between MotA chain 2 and 3, from the CI helix until the MotB chain 1, according to the mutagenesis data and the conformational changed observed in this study. In order to consider the flexibility of MotA chain 1 F186, the residue was ignored for the calculation. From the resulting channels, the one with best correlation to the biological data was selected.

Salmonella enterica strains and cultivation conditions

Salmonella enterica serovar Typhimurium LT2 (J. Roth) (ATCC 700720) (*S. enterica*) is one of the best-studied model systems for the function of the bacterial flagellum and was therefore used for our motility experiments. The *Se*MotAB clean deletion (Δ*motAB*) and *Se*MotA/MotB amino acid point mutants were generated in *S. enterica* LT2 using the λ-RED homologous recombination system (Karlinsey, 2007; Datsenko and Wanner, 2000) and pET11a-*Se*MotA-*Se*MotB-3C-TSII (constructed as described for the constructs used for cryo-EM) or *S. enterica* genomic DNA as template. The use of chromosomal point mutants leaves the native promoter intact and modifies only the respective codons, expectedly resulting in similar expression levels to wild-type. All mutants have been sequenced. *S. enterica* strains were grown at 37°C in LB.

Motility assays

Swimming motility was determined using tryptone broth (TB)-based soft agar plates containing 0.3% agar. Plates were inoculated with 2 μl overnight cultures or using a pin tool (V&P Scientific) and incubated 3–4 hours at 37°C. Diameters of the motility swarm were measured using ImageJ (Schneider et al., 2012) (NIH) and normalized to the wild-type.

Growth assays

S. enterica overnight cultures were diluted 1:100 in 96-well plates and the OD_{600} was measured in a microplate reader (Tecan) every 10 min for 8 hours with a brief shaking interval before each measurement. Growth rates were determined using GrowthRates 4.3 (Hall et al., 2014) with correlation coefficient $R > 0.995$.

Figure preparation

Figures were prepared using UCSF Chimera (Pettersen et al., 2004), UCSF ChimeraX (Goddard et al., 2018), GraphPad Prism 8 (GraphPad Software) and Illustrator (Adobe). Movies were prepared with UCSF ChimeraX, Premiere Pro (Adobe) and Keynote (Apple).

QUANTIFICATION AND STATISTICAL ANALYSIS

All values reported for the motility assays are the average of at minimum five independent replicates from separate experiments with the number of replicates indicated in the figure legends. Error bars represent SD as indicated in the corresponding figure legends. Statistical analysis of swimming diameter data relative to the wild-type was performed using unpaired, two-tailed Student's t test and significant differences are indicated in the figure with asterisks (* $p < 0.05$, ** $p < 0.01$, *** $p < 0.001$, ns non-significant).

Supplemental Figures

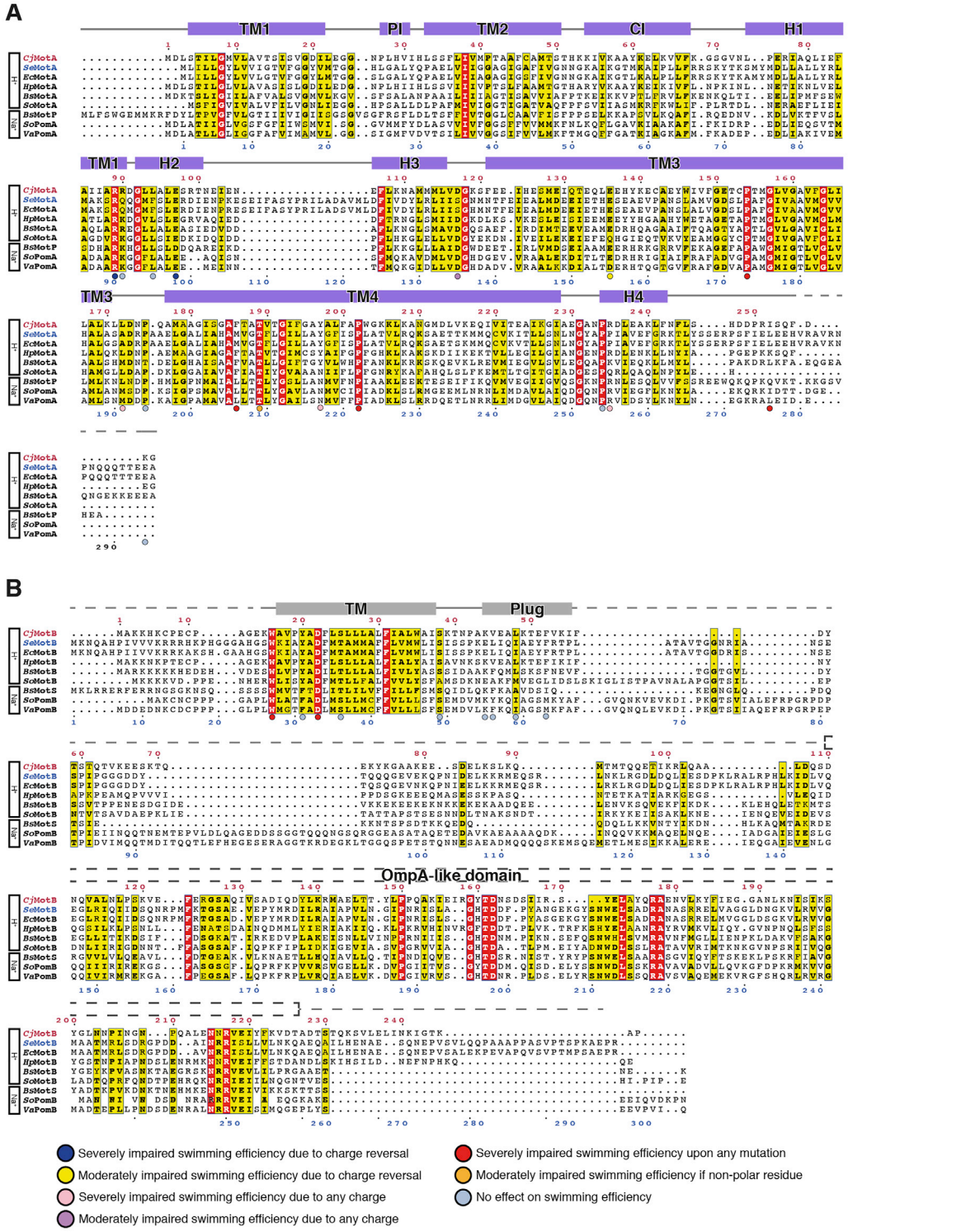

(legend on next page)

Figure S1. Sequence Alignment of MotA and MotB Homologs in Different Species, Related to Figures 2 and 3

(**A**) and (**B**) Multiple sequence alignment of MotA (A) and MotB (B). The proteins are subdivided into proton and sodium channels. Residue numbers above the sequences (red) correspond to the *C. jejuni* residue numbers, while residue numbers below the sequences (blue) correspond to those of *S. enterica*. Residues marked with a circle indicate residues mutated in *S. enterica*. α helices are indicated by solid boxes, the dashed lines indicate that the structure was not resolved in this study. The OmpA-like domain of MotB is also indicated above the alignment. Amino acids that are identical or partially conserved are colored red and yellow, respectively. *Cj*MotA identity to the sequences in the alignment ranges from 16.2% (*Se*MotA) to 58.9% (*Hp*MotA), similarity ranges from 37.4% (*Se*MotA) to 74.0% (*Hp*MotA). For *Cj*MotB, identity ranges from 13.9% (*Se*MotB) to 41.1% (*Hp*MotB), and similarity from 27.7% (*Se*MotB) to 58.9% (*Hp*MotB). Species abbreviations: *Cj*, *Campylobacter jejuni*; *Se*, *Salmonella enterica*; *Ec*, *Escherichia coli*; *Hp*, *Helicobacter pylori*; *Bs*, *Bacillus subtilis*; *So*, *Shewanella oneidensis*; *Va*, *Vibrio alginolyticus.*

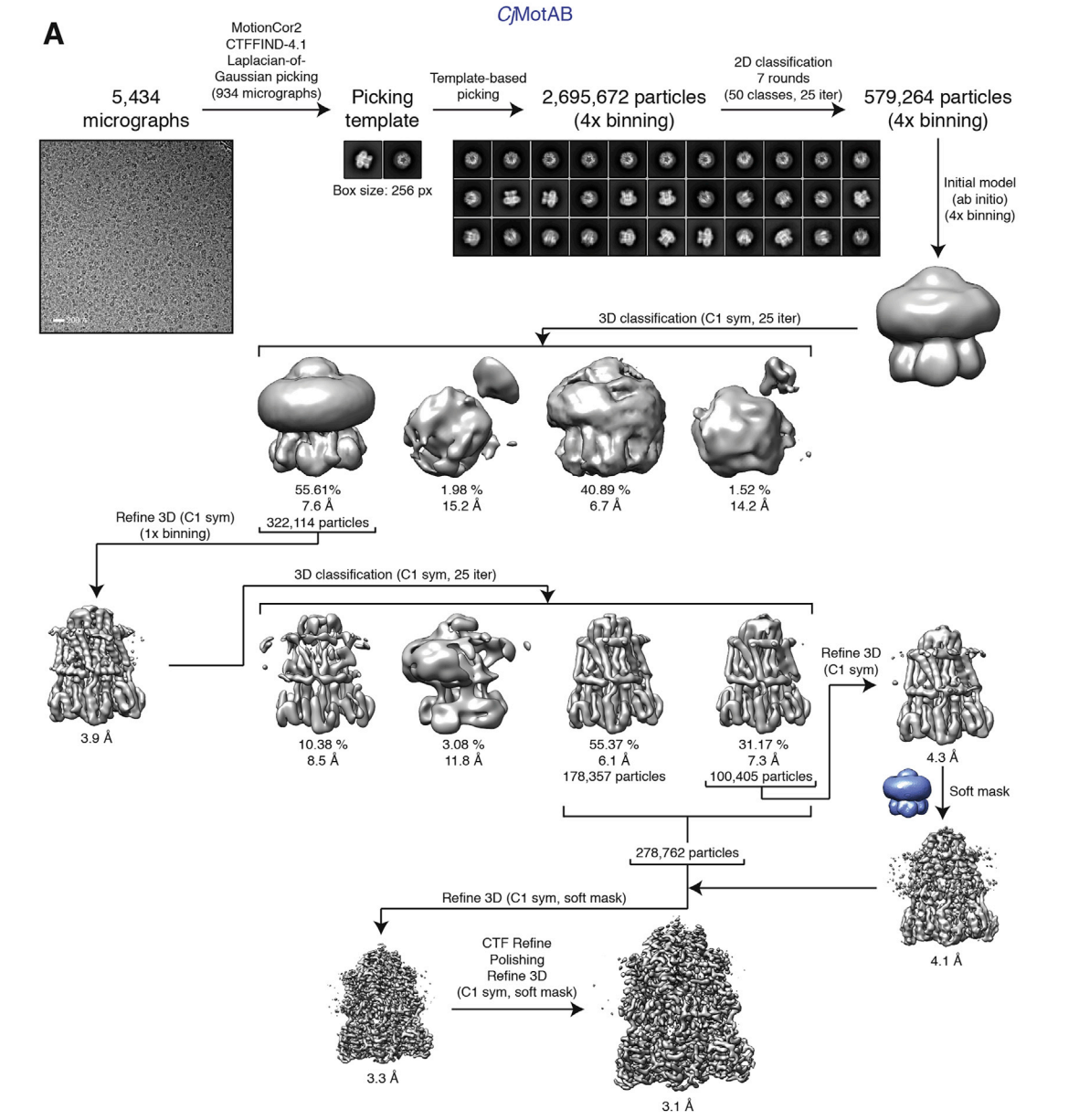

(legend on next page)

Figure S2. Cryo-EM of *Cj*MotAB, Related to Figure 1

(**A**) Flowchart of the data collection and processing pipeline in RELION that resulted in the final *Cj*MotAB Cryo-EM structure. 2,695,672 particles were picked from 5,434 micrographs. After 7 rounds of 2D classification, 579,264 particles were used to generate an initial model, followed by a 3D classification job with 4 classes. The best class containing 322,114 particles was unbinned and further 3D refined, obtaining a 3.9 Å resolution map. In order to improve resolution of MotB, another 3D classification was performed and class 4 was 3D refined, obtaining a 4.1 Å resolution map. To improve the resolution, particles from class 3 were also selected for another 3D refinement job. After masking, per-particle CTF refinement and Bayesian polishing, the map reached a resolution of 3.1 Å. (**B**) Cryo-EM density map of *Cj*MotAB colored by local resolution (in Å) estimated in RELION. (**C**) Euler angular distribution plotting for *Cj*MotAB. (**D**) 3D Fourier shell correlation (FSC) curves for *Cj*MotAB. Global resolution is estimated to be 3.1 Å at FSC = 0.143 (dashed line).

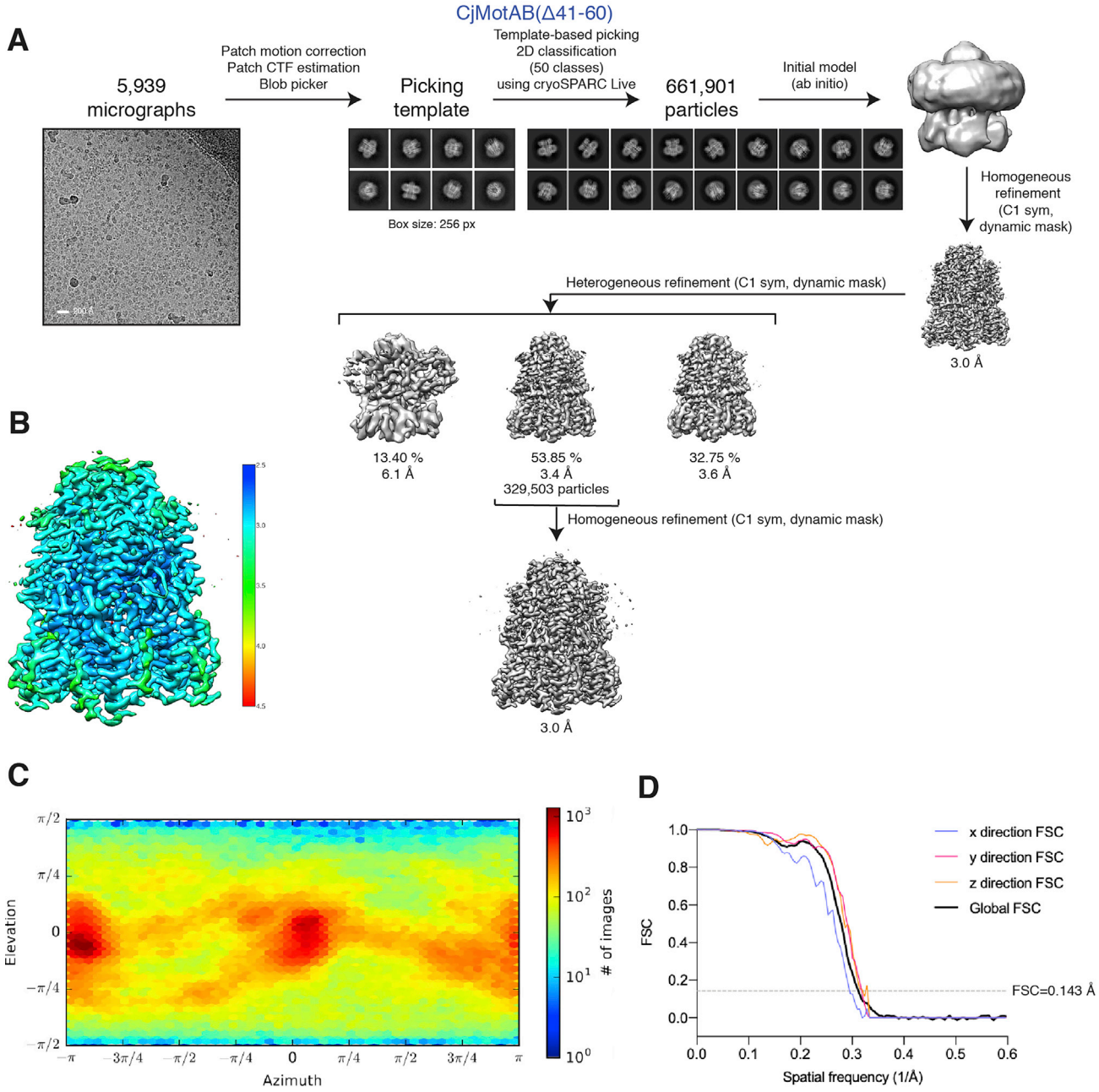

Figure S3. Cryo-EM of *Cj*MotAB(Δ41-60), Related to Figure 4

(**A**) Flowchart of the data collection and processing pipeline in cryoSPARC live that resulted in the final *Cj*MotAB(Δ41-60) cryo-EM structure. 5,939 micrographs were processed on-the-fly, and the 661,901 particles selected gave a 2.9 Å resolution map. In order to improve resolution of the TM domain of MotB, a heterogeneous refinement job was performed, and the best resulting volume (329,503 particles) was further refined, achieving a resolution of 3.0 Å. (**B**) Cryo-EM density map of *Cj*MotAB(Δ41-60) colored by local resolution (in Å) estimated in cryoSPARC. (**C**) Euler angular distribution plotting for *Cj*MotAB(Δ41-60) generated in cryoSPARC. (**D**) 3D Fourier shell correlation (FSC) curves for *Cj*MotAB(Δ41-60).

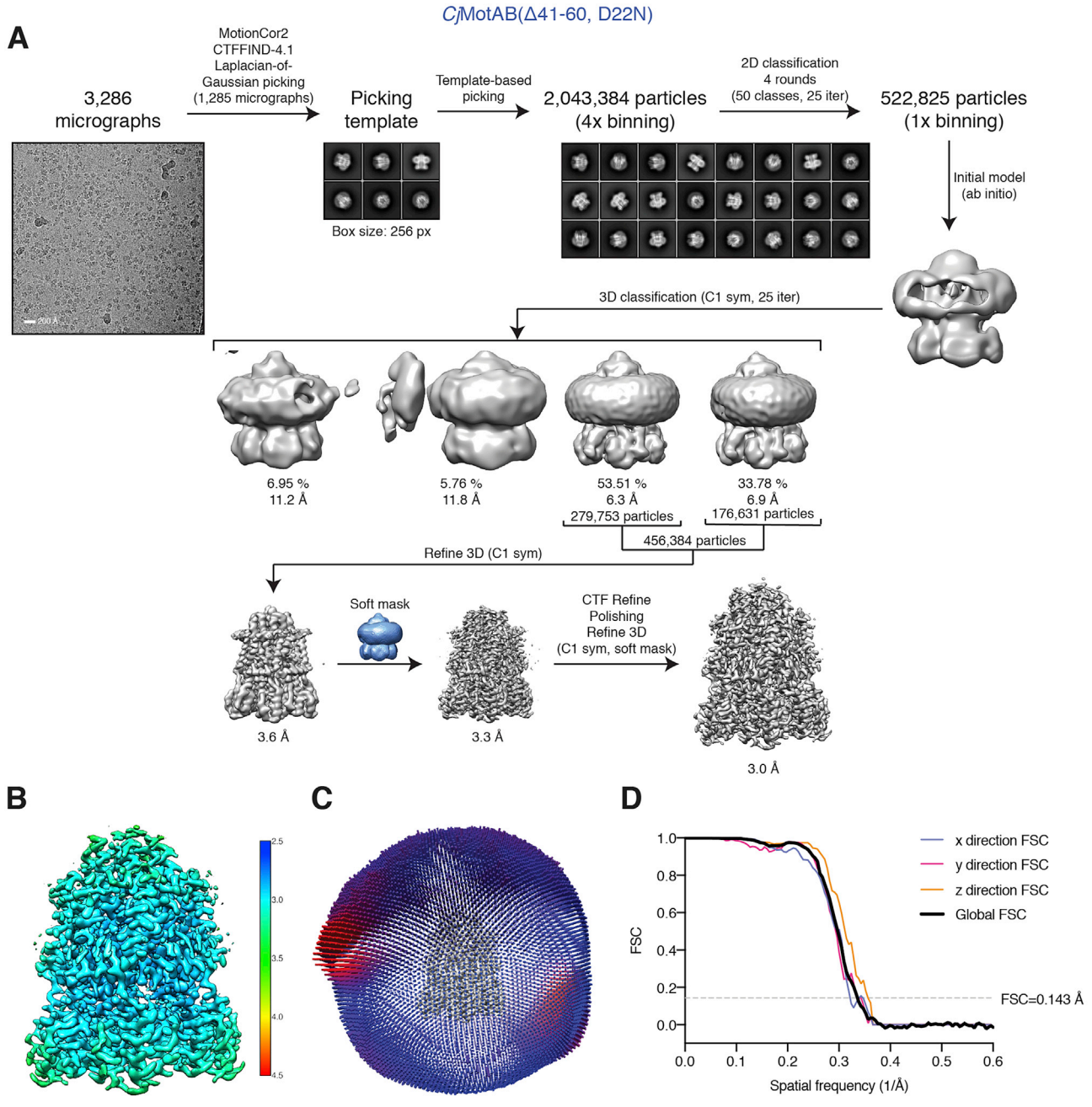

Figure S4. Cryo-EM of *Cj*MotAB(Δ41-60, D22N), Related to Figure 5

(**A**) Flowchart of the data collection and processing pipeline in RELION that resulted in the final *Cj*MotAB(Δ41-60, D22N) cryo-EM structure. 2,043,384 particles were picked from 3,286 micrographs. After 4 rounds of 2D classification, 522,825 particles were unbinned and used to generate an initial model and a following 3D classification with 4 classes. The best 2 classes (456,384 particles) were further 3D refined, obtaining a 3.6 Å resolution map. After masking, per-particle CTF refinement and Bayesian polishing, the map reached a resolution of 3.0 Å. (**B**) Cryo-EM density map of *Cj*MotAB(Δ41-60, D22N) colored by local resolution (in Å) estimated in RELION. (**C**) Euler angular distribution plotting for *Cj*MotAB(Δ41-60, D22N). (**D**) 3D Fourier shell correlation (FSC) curves for *Cj*MotAB(Δ41-60, D22N). Global resolution is estimated to be 3.0 Å at FSC = 0.143 (dashed line).

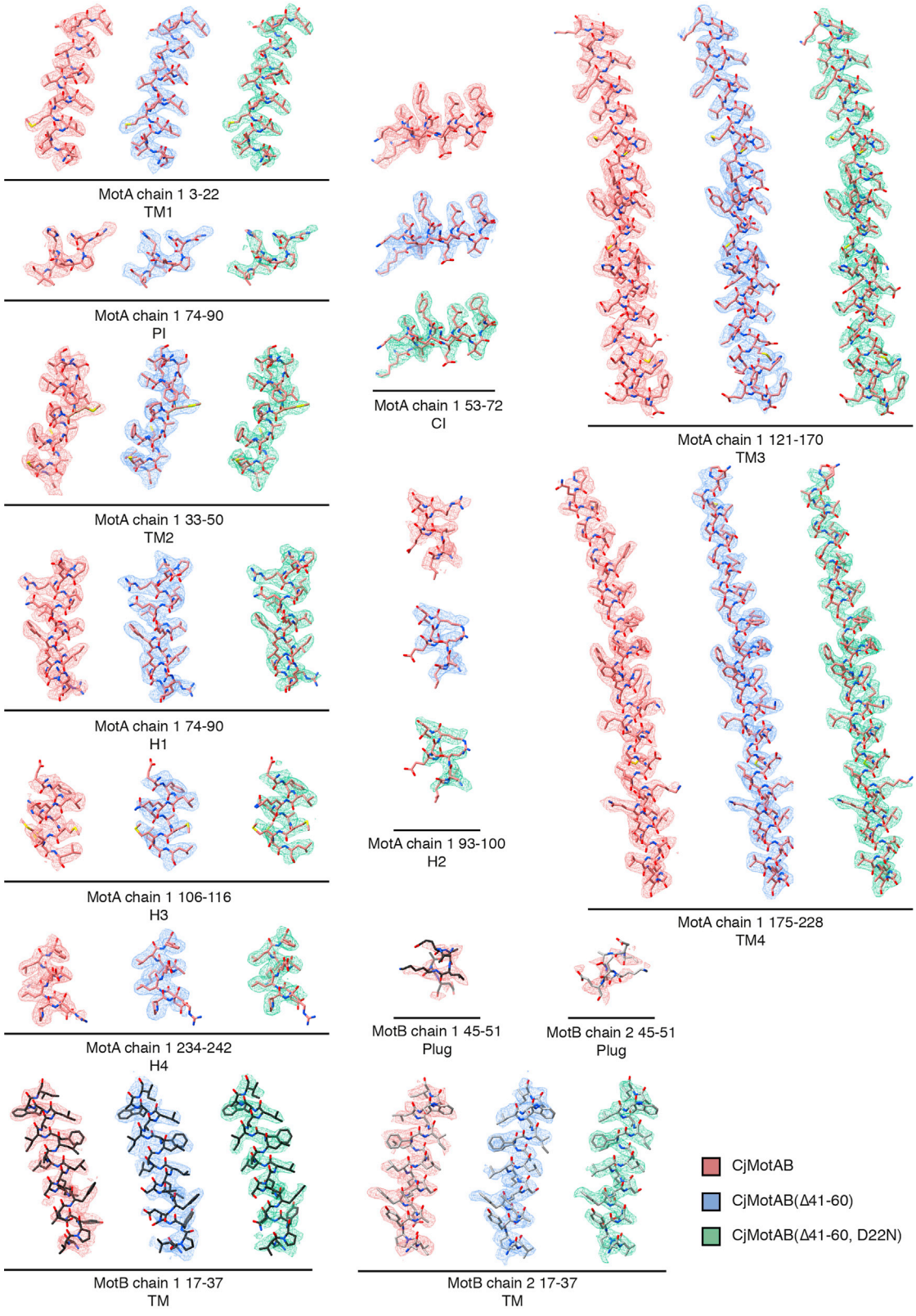

(legend on next page)

Figure S5. Fit of the *Cj*MotAB Atomic Models to the Cryo-EM Maps, Related to Figures 1, 4, and 5

Fragments of atomic models and the corresponding fragments of electrostatic potential maps, of the α helices of *Cj*MotA and *Cj*MotB for the *Cj*MotAB (red), *Cj*MotAB(Δ41-60) (blue) and *Cj*MotAB(Δ41-60, D22N) (green) structures.

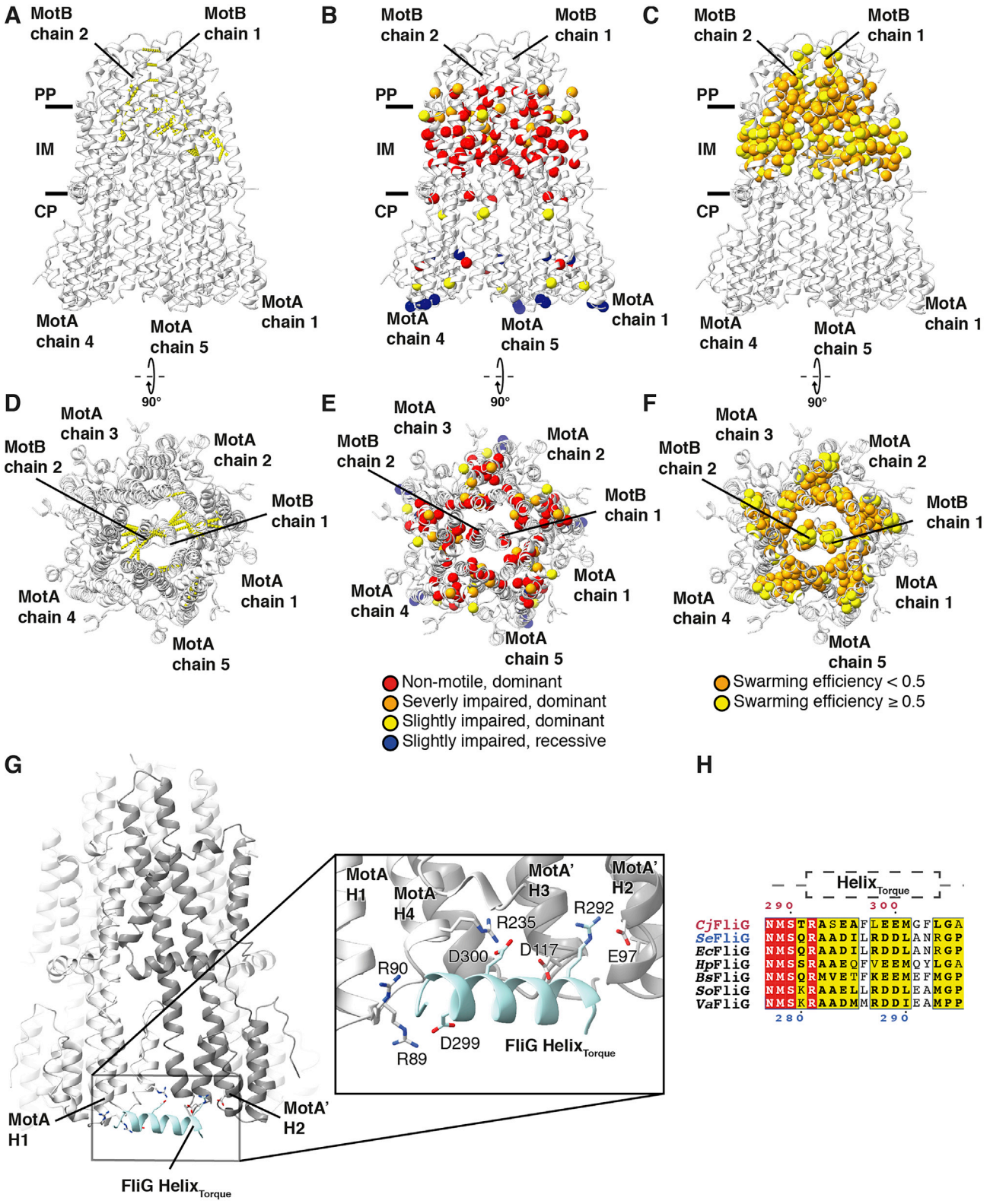

Figure S6. Validation of *Cj*MotAB Structure by Prior Functional Data and Modeling of MotA-FliG Interaction, Related to Figures 1 and 6

(A to C) Side views and (D to F) top views of the validation of the *Cj*MotAB structure, see STAR Methods for details. (**A**) and (**D**) Representation (shown as dotted yellow lines between the homologous C_α atoms) of *E. coli* MotAB (*Ec*MotAB) residues that can be crosslinked when they are mutated to cysteines (Braun et al.,

(legend continued on next page)

2004), mapped on the *Cj*MotAB structure. Of all possible crosslinks, only the result closest to 5 Å is displayed. A slice of the protein structure is shown. Note that the observed crosslinks are consistent with the expected C_α distances of cysteine crosslinks (5 Å), and that the crosslinks confirm the register of the MotB helices. (**B**) and (**E**) Mutational analysis for *Ec*MotA (Blair and Berg, 1991) and *Ec*MotB (Blair et al., 1991) plotted onto the *Cj*MotAB structure (represented as spheres on the position of the homologous C_α atom), colored by severity of the phenotype. Observe the distribution of phenotype severity according to the position in the structure. (**C**) and (**F**) Results of tryptophan scanning analyses for *Ec*MotA (Sharp et al., 1995a) and *Ec*MotB (Sharp et al., 1995b), plotted onto the *Cj*MotAB structure, represented as spheres on the position of the homologous C_α atom and colored by their impact on the swarming efficiency of *E. coli*. Note the different distribution of residues that can be more easily mutated to tryptophan (swarming efficiency > 0.5) (e.g., because they are interacting with the aliphatic chains of membrane lipids), versus those that cannot (swarming efficiency < 0.5) (e.g., because they are buried in the structure). (**G**) Modeling of the interaction between *Cj*MotA and the *Cj*FliG torque helix ($Helix_{Torque}$) (see STAR Methods) showing the interaction between the residues D299 and R292 of FliG with the residues R89 of one MotA subunit (light gray) and the residue E97 of the adjacent MotA subunit (light gray; MotA'). $Helix_{Torque}$: light blue. Charged residues on the interaction surface are shown in stick representation. (**H**) Conservation of FliG $Helix_{Torque}$. Top position numbers (red) refer to the *C. jejuni* FliG sequence, while bottom position numbers (blue) correlate with *S. enterica* FliG. $Helix_{Torque}$ is indicated by a dotted-line box. Amino acids that are identical or partially conserved are colored red and yellow, respectively. Species abbreviations: *Cj*, *Campylobacter jejuni*; *Se*, *Salmonella enterica*; *Ec*, *Escherichia coli*; *Hp*, *Helicobacter pylori*; *Bs*, *Bacillus subtilis*; *So*, *Shewanella oneidensis*; *Va*, *Vibrio alginolyticus*. (**I**) Schematic representation of the top of the rotor and the stator in *S. enterica*. The rotor has been shown as a 450 Å disc representing the measured distance (by the authors of the present study) at the top of the C-ring (expected to be the location of FliG $Helix_{Torque}$) of the wild-type rotor (Sakai et al., 2019). The expected FliG stoichiometry (34-fold) is represented by splitting up the disc in 34 equally-sized slices, one of which is colored in light blue. The stator unit is represented as a disc of diameter 75 Å, the measured diameter of the stator unit at its cytoplasmic region. The 5-fold stoichiometry and pseudo-symmetry of MotA is represented by its division into 5 equally-sized slices with thick black lines. The slices are subdivided into two to represent the proposed movement upon proton or hydronium transport in 36° steps as discussed in the text and in Figure 7. One of the five large slices of the stator unit is colored: one sub-slice is colored in purple, the other in light purple.

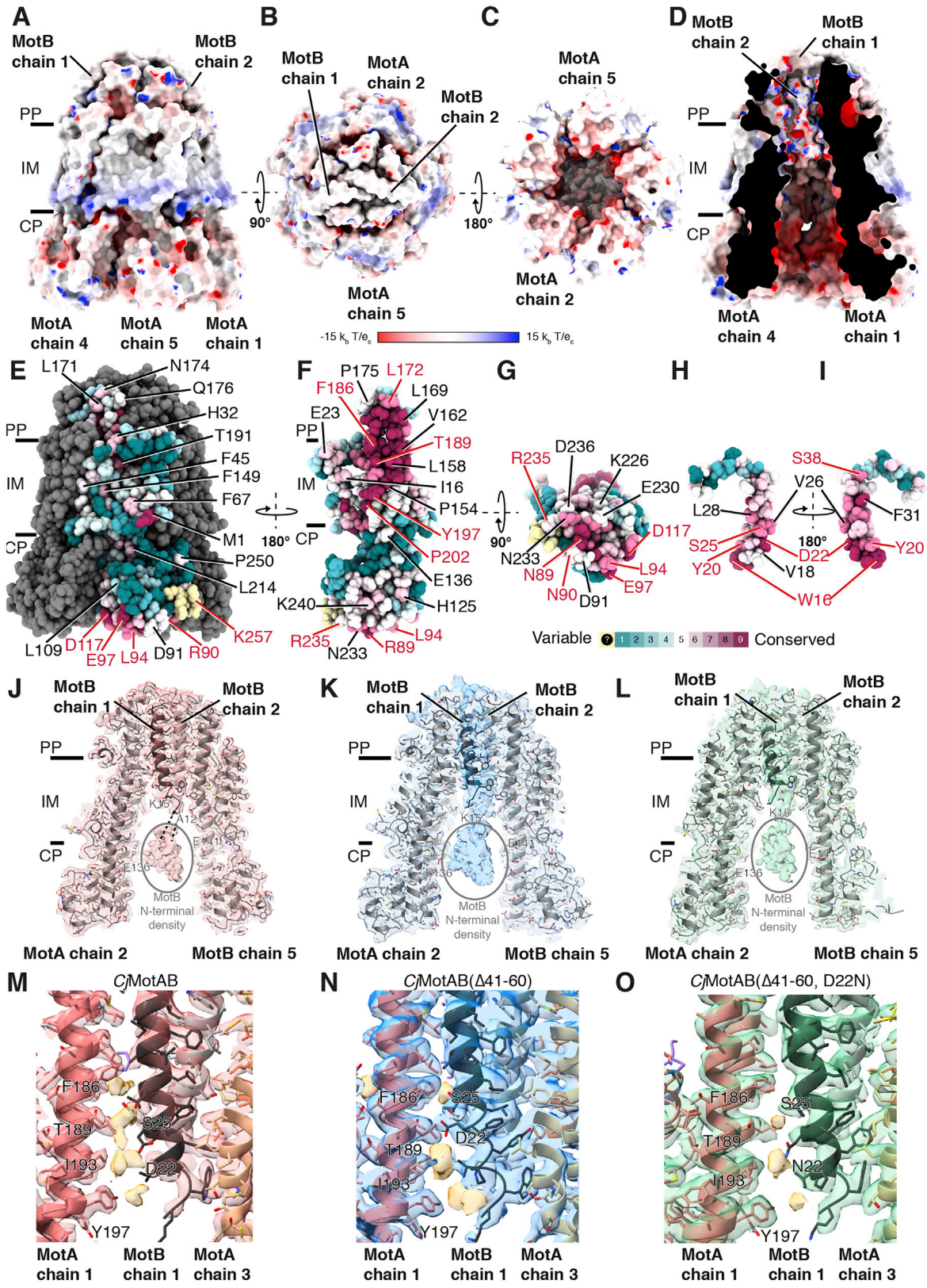

(legend on next page)

Figure S7. Charge and Surface Conservation of *Cj*MotAB, Density for the N-Terminal Region of *Cj*MotB, and Putative Solvent Molecules in the Channel, Related to Figures 1, 2, 3, 4, 5, and 6

(A to D) Exposed surface of MotAB from the side (A), top (B), bottom (C) and as a sliced side view (D) colored according to its electrostatic surface potential, calculated with APBS. For this calculation, MotA pentamer and MotB dimer electrostatic surface potentials were calculated separately and then joined in the same image to overcome limitation on grid size of the APBS software at the protein interfaces. (Jurrus et al., 2018). (**E**) to (**I**) Conservation (calculated with ConSurf (Ashkenazy et al., 2016)) of the surface residues of MotA from external side (E), internal side (F) and bottom (G); and of MotB from both sides (H-I). Atom representation of the model colored by conservation. All residues with a ConSurf conservation of ≥ 5 have been labeled. Homologous residues mutated in this study in *S. enterica* are labeled in red. (**J**) to (**L**) Representation of the *Cj*MotAB (J), *Cj*MotAB(Δ41-60) (K), and *Cj*MotAB(Δ41-60, D22N) (L) electrostatic potential maps at low threshold, together with the ribbon model representation with side chains of the corresponding atomic models, to illustrate the non-modeled density corresponding to the MotB N-terminal region. (**M**) to (**O**) Representation of *Cj*MotAB (M), *Cj*MotAB(Δ41-60) (N), and *Cj*MotAB(Δ41-60, D22N) (O) channels and putative solvent molecules. Density not modeled with atomic model, which is thought to correspond to solvent molecules (such as water) has been colored in pale yellow. CP, cytoplasm; IM, inner membrane; PP, periplasm.